POLITECNICO
MILANO 1863

SCUOLA DI INGEGNERIA INDUSTRIALE
E DELL'INFORMAZIONE

Thermochemical and Mechanical Behaviour of Carbon Fibre Reinforced Composite Laminates Subjected to Manufacturing Induced Cure Deviations

Tesi di Laurea Magistrale in
Materials Engineering and Nanotechnology-
Ingegneria dei Materiali e Nanotecnologie

Author: **Alessandro Garelli**

Student ID: 247333
Advisor: Prof. Roberto Frassine
Co-advisors: Marco Contino
Academic Year: 2024-2025

Abstract

Autoclave cure interruptions represent a critical manufacturing risk for aerospace composite structures. This thesis investigates the impact of an unplanned cure interruption on the thermochemical state and mechanical performance of an aerospace-grade Carbon Fibre Reinforced Polymer (CFRP) woven prepreg (Toray TC250/M46J 2×2 twill).

Two laminate batches were examined: a Baseline Cure (BC) and a Deviated Cure (DC). BC followed the manufacturer's recommended cure cycle; DC was subjected to an interruption during the 130 °C hold followed by a restart of the recommended cure cycle several days later. The study assesses these cure states by comparing their performance with the aerospace service temperature range (−50 °C to +150 °C) and the minimum material allowables set by the material Technical Process Specification (TPS).

The study combined thermochemical and thermomechanical indicators (DSC, TMA, DMA) with mechanical tests (compression, impact, Compression After Impact (CAI)).

The results showed that DC suffered substantial undercure ($DoC \approx 86\%$) compared to BC ($DoC \approx 98\%$). Consequently, DC exhibited a depressed T_g (140 °C) compared to BC (180 °C), failing the TPS minimum requirement of 175 °C. The TMA for DC revealed a high through-thickness coefficient of thermal expansion (up to 204.4×10^{-6} °C^{-1}) and increased scatter, indicating chemical and structural heterogeneity. The determination of the constituent content excluded major differences in fibre/resin fraction between batches.

Mechanically, room temperature compression properties remained stable for both batches, meeting TPS minimums despite increased scatter in DC. At 120 °C, the DC batch showed marked reductions in compressive strength and failure modes consistent with matrix softening. Impact testing revealed a typical residual strength decay. Although CAI performance was similar at 9.5 J, DC performance dropped by 13% at 18 J. Furthermore, the high temperature CAI for DC was 10–20% lower than the room temperature values.

Keywords: CFRP; autoclave cure interruption; differential scanning calorimetry; thermo mechanical analysis; dynamic mechanical analysis; CFRP compression testing; low-velocity impact; compression after impact.

Abstract in lingua italiana

Le interruzioni del ciclo di cura in autoclave rappresentano un rischio produttivo critico per le strutture aerospaziali in materiale composito. Questa tesi analizza l'impatto di un'interruzione non pianificata nel ciclo di cura sullo stato termochimico e sulle prestazioni meccaniche di un prepreg tessuto in CFRP di grado aerospaziale (Toray TC250/M46J 2×2 twill).

Sono stati confrontati due lotti: un Baseline Cure (BC), prodotto secondo il ciclo raccomandato, e un Deviated Cure (DC), interrotto durante il mantenimento a 130 °C e riavviato secondo il ciclo raccomandato dopo alcuni giorni. Lo studio valuta tali stati rispetto ai requisiti operativi aerospaziali (da −50 °C a +150 °C) e ai valori minimi ammissibili definiti dalla Specifica Tecnica di Processo (TPS) del materiale.

L'indagine ha combinato indicatori termochimici e termomeccanici (DSC, TMA, DMA) con prove meccaniche (compressione, impatto e compressione dopo impatto (CAI)).

I risultati indicano per il lotto DC una marcata sottopolimerizzazione ($DoC \approx 86\%$) rispetto a BC ($DoC \approx 98\%$). Di conseguenza, DC ha mostrato una T_g ridotta (140 °C) rispetto a BC (180 °C), fallendo il requisito minimo TPS di 175 °C. La TMA ha rivelato per DC un elevato coefficiente di espansione termica in direzione trasversale (fino a 204.4×10^{-6} °C^{-1}) e maggiore dispersione, segnali di eterogeneità chimica e strutturale.

Meccanicamente, le proprietà di compressione a temperatura ambiente sono rimaste stabili per entrambi i lotti, soddisfacendo i requisiti minimi delle TPS nonostante la maggiore dispersione in DC. Tuttavia, a 120 °C, il lotto DC ha mostrato riduzioni significative della resistenza e modalità di frattura coerenti con l'ammorbidimento della matrice. Le prove a CAI hanno evidenziato prestazioni simili a $E_i = 9.5$ J, ma una riduzione del 13% per DC a $E_i = 18$ J. Inoltre, la resistenza CAI ad alta temperatura per DC è risultata inferiore del 10–20% rispetto ai valori a temperatura ambiente.

Parole chiave: CFRP; interruzione della cura in autoclave; calorimetria a scansione differenziale; analisi termo meccanica; analisi dinamico meccanica; compressione di CFRP; impatto a bassa velocità; compressione dopo impatto.

Contents

List of Figures

List of Tables

List of Symbols

Variable	Description	SI unit
A	Specimen Area	m^2
A_r	Fibre Areal Weight	g/m^2
b	Empirical Parameter for Machine Compliance	–
d_m	Machine Compliance Displacement	mm
$d_{\max}$	Maximum Deflection	mm
d_{ns}	Non-Seating Displacement Term of d_m	mm
d_{raw}	Raw Crosshead Displacement	mm
d_s	True Specimen Deformation	mm
DoC	Degree of Cure	–
E'	Storage Modulus	GPa
E''	Loss Modulus	GPa
E_a	Absorbed Energy	J
E_c	Critical Damage Threshold (Zone A to Zone B)	J
E_i	Nominal Impact Energy	J
E_j	Impact Energy at Start Of Zone C	J
$E_{\max}$	Peak Value of E_a–t Curve	J
F_{CAI}	Residual Compressive Strength from CAI	MPa
$F_{\max}$	Maximum Contact Force	N
F_{cu}	Compressive Strength	MPa
g	Gravitational Acceleration	m/s^2
H	Drop Height of Impactor	m
h	Specimen Thickness	mm
H_r	Residual Cure Enthalpy (Cured Laminates)	J/g
H_t	Total Cure Enthalpy (Uncured Reference)	J/g

Continued on next page

List of Symbols – continued from previous page

Variable	Description	SI unit
K	Linear Compliance Coefficient	mm/N
k	Empirical Parameter for Machine Compliance	–
L_0	Initial Specimen Length at Start Of TMA Scan	mm
m	Impactor Mass	kg
M_f	Final Fibre Mass (After Digestion and Drying)	g
M_i	Initial Specimen Mass (Before Digestion)	g
m_{pr}	Prepreg Areal Weight	g/m^2
N	Number of Plies of Panel Reference	–
P	Applied Load	N
P_c	Critical Threshold Force For Onset of Damage	N
$P_{\max}$	Maximum Load in Compression	N
P_n	Penetration Threshold Energy	J
P_r	Perforation Threshold Energy	J
T	Temperature	°C
t	Cured Ply Thickness	mm
$\tan\delta$	Damping Factor (E''/E')	–
T_g	Glass Transition Temperature	°C
T_{g0}	Glass Transition Temperature of Uncured Monomer	°C
$T_{g\infty}$	Glass Transition Temperature of Fully Cured Network	°C
v_i	Initial Impact Velocity	m/s
v_r	Rebound Velocity	m/s
W_m	Resin Mass Fraction (Resin Content)	wt%
α_g	Apparent CTE in Glassy Region ($T < T_g$)	$°C^{-1}$
α_r	Apparent CTE in Rubbery/Post-Transition Region ($T > T_g$)	$°C^{-1}$
α_T	Instantaneous Linear Thermal Expansion Coefficient	$°C^{-1}$
ε_{cu}	Strain at Failure in Compression	–
λ	Structure-Dependent Parameter in DiBenedetto Equation	–
ρ_c	Density of Panel Reference	g/cm^3
ASTM	American Society for Testing and Materials	–
BC	Baseline Cure	–

Continued on next page

List of Symbols – continued from previous page

Variable	**Description**	**SI unit**
BVID	Barely Visible Impact Damage	–
CAI	Compression After Impact	–
CFRP	Carbon Fibre Reinforced Polymer	–
CLC	Combined Loading Compression	–
CTE	Coefficient of Thermal Expansion	–
DC	Deviated Cure	–
DGEBA	Diglycidyl Ether of Bisphenol A	–
DMA	Dynamic Mechanical Analysis	–
DSC	Differential Scanning Calorimetry	–
EPD	Energy Profile Diagram	–
LDM	Lateral through Damage in Middle (Failure Mode)	–
NDE	Non Destructive Evaluation	–
PAN	Polyacrylonitrile	–
SBS	Short Beam Shear	–
TMA	Thermo Mechanical Analysis	–
TPS	Technical Process Specification	–

1 State of the Art and Background

Composite materials, especially Carbon Fibre Reinforced Polymers (CFRPs), are widely used in aerospace structures because they offer high specific stiffness and strength, good fatigue and corrosion resistance, and excellent dimensional stability. Their performance depends strongly on manufacturing conditions, particularly the curing cycle applied to the matrix. This thesis investigates the thermochemical and mechanical consequences of manufacturing induced cure deviations in an aerospace-grade woven CFRP laminate.

To interpret the experimental work in this thesis, it is therefore necessary to connect the roles of fibre and matrix, the kinetics of epoxy cure, and the resulting network structure, with laminate-level performance.

This chapter summarises the key background on aerospace CFRPs and explains why epoxy matrices are sensitive to cure cycle variations before introducing the industrial context of this study.

1.1. CFRP in Aerospace

CFRPs consist of high-strength carbon fibres embedded in a thermoset or thermoplastic polymer matrix.

The fibres are the primary load-bearing constituents and typically carry most of the axial load. Their stiffness, strength, low density, and thermal stability largely determine in-plane mechanical behaviour.

The matrix binds the fibres, provides rigidity and shape, transfers the load to the fibres, and influences toughness, damage tolerance, and failure mode. Consequently, the choice of matrix and its processing history significantly affect the properties of the composite material [1, 2].

In the aerospace industry, CFRPs are widely used in aircraft secondary structures and con-

trol surfaces (trim tabs, spoilers, rudders, doors), and increasingly in larger load-carrying assemblies such as vertical and horizontal stabilisers, wings, and fuselage structures. Additional applications include radomes, fairings, and landing-gear doors. Beyond aircraft, CFRPs are also used in space systems where low mass and dimensional stability are critical [2, 3].

1.1.1. Carbon Fibres: Characteristics and Properties

Carbon fibres are the reinforcing phase in CFRPs. They are composed of small crystallites of turbostratic graphite. As shown in Figure 1.1, graphite consists of hexagonal planar carbon layers. Strong covalent bonding within each layer and weaker Van der Waals interlayer forces lead to pronounced anisotropy: properties parallel to the basal planes are much higher than those normal to them [3].

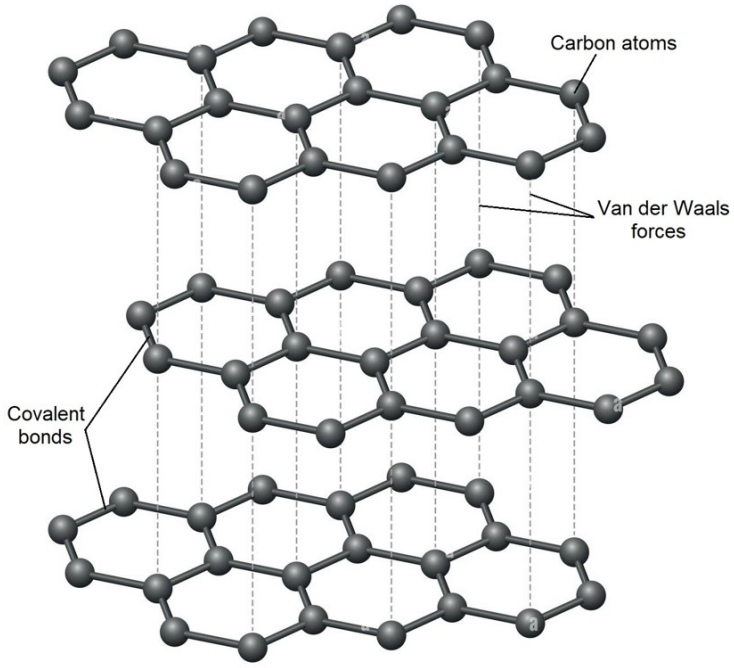

Figure 1.1: Crystalline structure of graphite.

Carbon and graphite fibres are commonly produced from polyacrylonitrile (PAN) fibre precursors. After wet-spinning, the precursor is stabilised (oxidised) at elevated temperature (typically 200–400 °C) and then carbonised. Carbonisation is a high-temperature treatment (approximately 1000–3000 °C) that removes non-carbon elements and promotes alignment of the carbon-rich structure. High-strength fibres are produced at lower treatment temperatures (below about 1500 °C), while high-modulus fibres require higher temperatures (graphitisation) [2, 4].

To promote adhesion to the polymer matrix, fibres are surface treated (oxidation/etching) and coated with a sizing compatible with the target resin system. Although laminate stiffness and strength are largely governed by fibre properties, matrix support and out-of-plane performance can be equally critical for structural integrity.

At the macroscopic scale, carbon fibres are supplied as tows: bundles of filaments wound onto packages, often with kilometre-scale lengths. Tows may be woven into fabrics such as plain weave, twill, and satin, as shown in Figure 1.2. Woven fabrics can drape over curved surfaces with reduced wrinkling, which is advantageous for complex aerospace geometries [3].

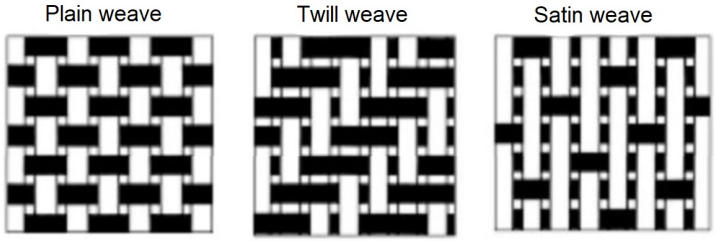

Figure 1.2: Different types of woven fabrics.

Typical aerospace carbon fibre properties are summarised in Table 1.1, depending on precursor type and heat treatment conditions [2].

Table 1.1: Properties of carbon fibres and steel.

Property	**Carbon Fibre (High Modulus)**	**Carbon Fibre (High Strength)**	**Steel**
Diameter [μm]	6-8	6-8	–
Density [g/cm^3]	1.8-2	1.7-1.9	7.7-7.9
Tensile Modulus [GPa]	350-450	200-300	190-210
Tensile Strength [GPa]	1.5-2.5	2.5-5	0.34–2.1
Specific Modulus [GPa/(g/cm^3)]	175-250	110-170	24-30
Specific Strength [GPa/(g/cm^3)]	0.75-1.4	1.5-3	0.04–0.27
Melting Point [°C]	$>$ 3500	$>$ 3500	$\approx$ 1480
Elongation at Break [%]	1-2	0.6-1	5–25
Relative Cost	High	High	High–Medium

1.1.2. Epoxy Resins: Characteristics and Properties

Epoxy resins are the most widely used matrix systems in structural CFRPs because they combine good mechanical performance, chemical resistance, dimensional stability, and practical processing behaviour. In fact, they can be processed at low viscosity before crosslinking, which facilitates fibre impregnation and lay-up.

Typical unfilled epoxy thermoset properties are given in Table 1.2 [2].

Table 1.2: Typical unfilled thermosetting resin properties.

Resin Material	Density [g/cm^3]	Tensile Modulus [GPa]	Tensile Strength [MPa]
Epoxy	1.2–1.4	2.5–5.0	40–70

Epoxy resin formulations are generally prepared in two stages: a prepolymer containing epoxide groups is produced, and then the prepolymer is mixed with a curing agent (hardener) to initiate crosslinking.

A common prepolymer is Diglycidyl Ether of Bisphenol A (DGEBA), which contains two epoxide groups per molecule (Figure 1.3). Each epoxide group is a three-membered ring consisting of two carbon atoms and one oxygen atom. The curing agent may be an amine, anhydride, or other reactive species.

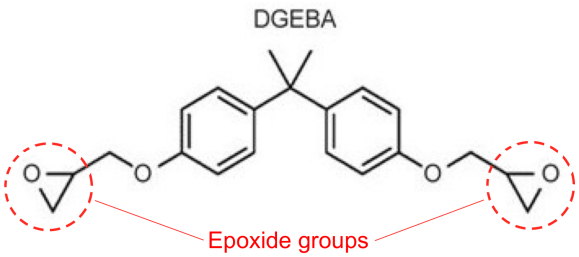

Figure 1.3: DGEBA molecule.

During curing, covalent bonds form between epoxy and hardener molecules, progressively building a three-dimensional network under controlled temperature and pressure. As crosslink density increases, chain mobility decreases and, as a result, the resin cannot be remelted. A higher crosslink density increases stiffness, glass transition temperature (T_g), and thermal stability, but can reduce ductility [5, 6]. Post-curing at higher temperature is often used to increase the Degree of Cure (DoC) and increase T_g. Since crosslink density

depends on cure temperature and time, significant deviations from the specified thermal profile can change the final network structure and, therefore, laminate performance. This sensitivity is discussed further in Section 1.2.

Because matrix-dominated properties are strongly dependent on network structure, the final composite response is sensitive to DoC, crosslink density, and void content.

Additives (catalysts, inhibitors, and flame retardants) are included in practical formulations to meet processing and performance requirements. Since epoxies are inherently brittle, aerospace-grade systems are often toughened using thermoplastic additives, rubbers, or particulate fillers to improve damage tolerance and impact resistance [2].

Matrix-dominated properties degrade as the temperature approaches or exceeds T_g, which limits standard epoxy CFRPs to service temperatures below about 120 °C. Moisture absorption reduces T_g, further restricting the allowable service temperature. Higher temperature systems can reach service temperatures of around 200 °C, at increased cost [2, 3].

1.1.3. Prepregs: Lamination Process and Cure Cycles

Prepregs are resin-impregnated fibres or fabrics supplied in sheet form with a controlled fibre-to-resin ratio. They are delivered in rolls, stored under refrigeration to limit premature cure, and used in manual or automated layup.

Prepregs provide consistent properties because the volume fraction of the fibre and the resin content are tightly controlled. They also remove on-site resin mixing, reducing variability and common processing errors.

Typical properties of a fabric prepreg are listed in Table 1.3 [2].

Table 1.3: Typical properties of fabric (plain weave) thermoset prepreg materials.

Property	**Carbon (AS4) + Epoxy**
Fibre Volume Fraction [%]	57–63
Processing Temperature [°C]	120
Tensile Modulus [GPa]	55–62
Tensile Strength [MPa]	517–885
Compressive Modulus [GPa]	48–65
Compressive Strength [MPa]	450–655
Shelf Life [months]	6

As a result of this control, prepreg laminates can achieve reliable mechanical performance compared to less-controlled manufacturing routes. The main drawbacks are the higher material and processing costs, the lack of high-volume lamination methods, the longer lamination times, and the limited recyclability for thermoset systems.

Prepregs are manufactured by solvent impregnation or hot-melt technology. Solvent impregnation uses a resin solution to reduce viscosity for wetting; however, solvent removal introduces environmental and handling concerns. Hot-melt technology avoids solvents by applying the resin in a molten or highly viscous state, improving environmental compatibility but making the complete wetting of the fibre more challenging [2].

In aerospace manufacturing, the process chain includes ply cutting and layup (with strict control of fibre orientation), intermediate debulking to reduce voids and improve interply contact, vacuum bagging to evacuate air and volatiles, and autoclave curing. During autoclave curing, vacuum and external pressure are applied with a prescribed temperature cycle to consolidate the laminate and complete curing. More details are provided in Section 2.2.

Thermoset prepregs typically require cure cycles of 1 to 8 h due to relatively slow reaction kinetics. To increase production rates, rapid-curing prepregs are under development.

The cure cycle (heating/cooling rates, dwell temperatures and times, and applied pressure) controls the viscosity, crosslinking, and network development. Manufacturer Technical Process Specifications (TPS) cure cycles are designed to achieve complete cure, minimise void content (typically $< 1\%$), and deliver properties consistent with the qualification data [3, 5].

1.2. Matrix-Dependent Properties

The polymer matrix plays a central role in laminate behaviour. Although fibres carry most of the axial load, the matrix governs other properties such as compression strength, toughness, impact damage resistance, and failure mode.

In a laminate, matrix loads must be transferred to the fibres through the fibre-matrix interface. Effective wetting and adhesion, therefore, enable stress transfer between plies and reduce the risk of delamination under service loads.

Fracture behaviour also depends on the strength of the interface: a weak interface typically reduces stiffness and strength, but can increase fracture resistance through energy dissipation mechanisms, whereas a strong interface promotes stiffness and strength, but

can lead to more brittle fracture [3].

1.2.1. Influence of the Cure Cycle on Composite Behaviour

Matrix-dominated properties, such as compressive strength and impact damage resistance, are highly sensitive to the network structure of the cured resin. This sensitivity is often amplified in woven laminates, where the waviness of the fibre and the resin-rich regions create local stress concentrations and increase the dependence on the thermal history.

Several studies indicate that cure cycles can be accelerated within an appropriate process window. For example, Dong et al. investigated a rapidly out-of-autoclave cured epoxy prepreg reinforced with T800 carbon fibres. They reported that a higher heating rate reduced the cure time by approximately 35% without preventing full cure, and extending post-cure from 2 to 3 h did not produce a significant improvement in short beam shear strength [7].

Cure temperature has a clearer effect when it leads to undercure. Alavi-Soltani et al. studied a commercial carbon fibre/epoxy unidirectional prepreg processed in an autoclave using isothermal cure temperatures between 149 °C and 182 °C for 180 min (heating and cooling rates of 2.8 °C/min). Combined Loading Compression (CLC) and Short Beam Shear (SBS) tests showed that mechanical properties did not vary significantly over 160–182 °C. On the other hand, specimens cured at 149 °C exhibited an approximately 10% reduction in SBS strength and a change in the SBS failure mode towards interlaminar shear, consistent with insufficient inter-ply bonding under severe undercure [8].

Gernaat et al. reported that for another similar prepreg system (Cycom 5215 PW), the mechanical properties were essentially unchanged over an isothermal dwell temperature range of 93–127 °C. In contrast, curing at 82 °C led to marked reductions in the SBS and the CLC strengths and a shift in the failure mode towards delamination, indicating inadequate interlaminar integrity under severe undercure [9, 10]. Trends of reduced compressive strength at lower crosslink density have also been reported for other epoxy networks, while elastic modulus below T_g can remain comparatively insensitive [11].

Cure advancement also affects fibre–matrix bonding and resin stiffness. The longitudinal and transverse properties of similar prepreg systems increased with cure progression, consistent with strengthening of the interface and matrix [12]. Post-curing can further improve properties by increasing the degree of cure and T_g [13].

In summary, moderate variations in dwell temperature and limited reductions in cycle time (increased heating rate or reduced post-curing time) can be tolerated without significant

property changes, provided the laminate reaches an adequate final degree of cure [7, 14]. In contrast, severe undercure reduces interlaminar integrity, leading to lower strength and delamination-dominated failure [8–11].

Interruptions, unexpected cooldowns, or prolonged dwells at intermediate temperatures can slow or arrest polymerisation, lower the achievable T_g, and degrade resin-dominated performance. Whether properties are recoverable depends mainly on when the interruption occurs in relation to gelation/vitrification and whether a subsequent cure provides sufficient time and temperature to complete network formation.

1.2.2. Impact Damage and Residual Compressive Strength

In aerospace structures, polymer matrix composites are frequently exposed to low-velocity impact events during manufacturing, handling, maintenance, and service (e.g., dropped tools, ground equipment contact, runway debris). Although such impacts may leave only limited surface evidence, they can produce internal damage that degrades structural integrity, particularly under compressive loading. For this reason, understanding the main impact damage mechanisms and their link to residual Compression After Impact (CAI) strength is essential for a damage-tolerant design.

The low-velocity impact on laminated polymer matrix composites typically produces a combination of interacting damage mechanisms. A widely adopted classification identifies four major damage modes: (i) matrix-dominated, where cracking develops mainly within the resin and often parallel to the fibres under tension, compression, or shear; (ii) delamination, driven by interlaminar stresses at the interfaces of the plies; (iii) fibre-dominated, including fibre fracture in tension and fibre microbuckling/kinking in compression; and (iv) penetration and perforation, in which damage progresses to full thickness breakthrough of the laminate [15–17]. These mechanisms are not mutually exclusive: early matrix cracking frequently precedes and promotes delamination, while extensive fibre failure is generally associated with the transition towards penetration and perforation [15, 16].

In woven fabric composites, the yarns are inevitably crimped along their length due to the interlaced architecture. This crimp reduces fibre straightness and can lead to lower tensile and compressive properties, as well as poorer in-plane shear resistance, compared to unidirectional laminates [18]. Nevertheless, woven fabric laminates have also been reported to exhibit a lower maximum impact load but a smaller damage area, a higher ductility index, and higher residual (CAI) strength than unidirectional laminates. This highlights a potentially favourable response to damage of woven fabrics, despite reduced

in-plane efficiency [18].

At the damage initiation level, the first observable mechanisms are often matrix cracking and local fibre–matrix debonding. Cracks may initiate beneath and around the impactor contact region, particularly near the contact edges, where transverse shear stresses are high. These cracks are frequently inclined at approximately 45°, consistent with shear-driven cracking through the thickness [15, 16]. In addition to shear cracks, a distinct class of cracks can develop on the back face of the laminate: the so-called bending cracks, induced by tensile bending stresses, oriented vertically through the thickness [15]. For relatively long and thin plates, larger transverse deflection increases bending and membrane effects, making bending cracks in the lower plies more likely [15].

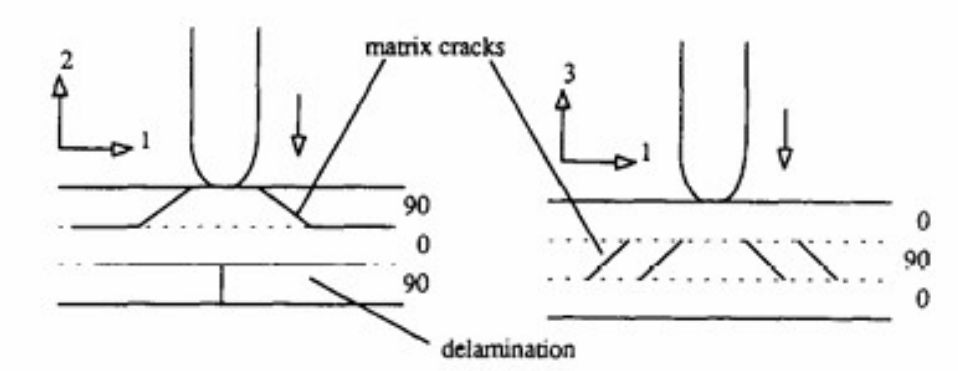

Figure 1.4: Schematic representation of early damage in an impacted composite plate. Left: transverse view. Right: longitudinal view.

A key consequence of matrix cracking is that it can trigger delamination. A delamination is a crack that propagates along the resin-rich interlaminar region between the plies (typically between plies of different fibre orientations), rather than within a single lamina [15]. Under transverse impact, delaminations are commonly oblong or "peanut-shaped", with their major axis often aligned with the fibre direction of the ply beneath the delaminating interface [15]. Delamination is strongly related to interlaminar stresses driven by bending and is amplified when there is a strong bending stiffness mismatch across the interface; therefore, interfaces such as 0°/90° are frequently associated with larger delaminated areas [15, 19]. Importantly, low-velocity impact delamination is generally observed only after a threshold severity and is often reported to occur in conjunction with matrix cracking: when an inclined shear crack reaches an interface, it can be arrested by the change in orientation of the ply and subsequently deflect along the interface, evolving into a delamination [15, 16]. Furthermore, delamination growth can exhibit different stability depending on its origin: delaminations associated with shear cracking can grow

in a more unstable manner, while those associated with bending cracks can grow more steadily with increasing load [15].

As the severity of the impact increases, fibre failure becomes more prominent. Fibre breakage can occur locally under the impactor due to high contact stresses and indentation effects (often dominated by transverse shear). Additional fibre failure may develop on the non-impacted face due to bending-induced tensile stresses [15, 16].

When fibre failure reaches a critical extent and can no longer sustain load transfer, the damage state transitions towards penetration and perforation, allowing the impactor to break through the laminate thickness [15, 17].

From a structural perspective, the main concern is that even Barely Visible Impact Damage (BVID) on the surface can cause a substantial reduction in residual properties (up to 50%), especially in compression [15, 17]. Post-impact compression is particularly critical because delamination divides the laminate into thinner sublaminates with reduced bending stiffness, promoting instability. Under compressive loading, delaminated regions can trigger (i) global buckling of the entire laminate, (ii) local buckling of a sublaminate, or (iii) mixed-mode instability; the governing mode often shifts from global towards local/mixed behaviour as the delamination size increases [15]. From a material perspective, toughened resin systems and thermoplastic modifications can mitigate matrix-dominated damage and delay delamination growth, thus improving damage tolerance [16, 17].

1.3. Industrial Context

The experimental work presented in this thesis was carried out during an internship at Persico Marine (Persico Group), in an industrial environment focused on the design and manufacture of high-performance composite structures for aerospace applications.

The internship activities were carried out in support of an industrial development program in the space sector. Due to confidentiality constraints, detailed information on the customer, vehicle architecture, and component geometry cannot be reported in this thesis. The discussion is therefore limited to the materials and process aspects that are necessary to motivate and interpret the experimental campaign.

Within this framework, mission-driven constraints (mass efficiency, manufacturing feasibility, and environmental compatibility) were translated into engineering design inputs. In particular, minimum material allowables and selection criteria were defined to account for manufacturing variability and damage tolerance, and to ensure compatibility with the expected operating environment (see Section 2.1).

2 | Experimental Details

2.1. Materials

Table 2.1 presents the Carbon Fibre Reinforced Polymer selected for the construction of the target structure. Material selection was guided by challenges of the space environment. Key constraints included compliance with restricted substance requirements, low outgassing to avoid contamination of sensitive surfaces, and compatibility with vacuum exposure. Additional drivers were mechanical performance, resistance to thermal cycling and radiation, bonding compatibility, and manufacturability with the selected processing route. This material was chosen based on its well-documented mechanical properties and qualification in previous aerospace missions.

The minimum material properties at room temperature of the selected CFRP are summarised in Table 2.2. Additionally, the target structure must maintain mechanical and thermal integrity across an operational temperature range of -50 °C to +150 °C, as defined by preliminary thermal analyses.

Table 2.1: Selected CFRP material specifications.

Specification	**Details**
Commercial Name	TC250-00 HM0122 40% M46J CAR200 2×2 1.25 m
Maker	Toray Advanced Composites
Fibre	Torayca M46J 200 gsm Fabric Twill 2×2
Resin	Toray TC250-00 HM0122 40%

Table 2.2: TPS material requirements at room temperature for the selected CFRP.

Property	Test Standard	Requirements
Resin Content	ASTM D3171	37–43 wt%
Glass Transition Temperature (T_g)	ASTM D7028	175 °C
Compression Strength 0°	ASTM D6641	290 MPa
Compression Modulus 0°	ASTM D6641	80 GPa
Tensile Strength 0°	ASTM D3039	655 MPa
Tensile Modulus 0°	ASTM D3039	90 GPa

This material is supplied as a 2×2 twill fabric prepreg with an areal weight of 200 g/m^2 (roll width 1.25 m). Since each 2×2 twill ply is balanced, the reinforcement within a ply is distributed between warp (0°) and weft (90°) tows (see Figure 2.1). The reinforcement is Torayca M46J, an MJ-type high-modulus carbon fibre (tensile modulus 436 GPa; tensile strength 4.2 GPa; fibre density 1.84 g/cm^3; nominal filament diameter 5 μm) [20]. The fibre is supplied with an epoxy-compatible sizing (50B, 1.0%) [20].

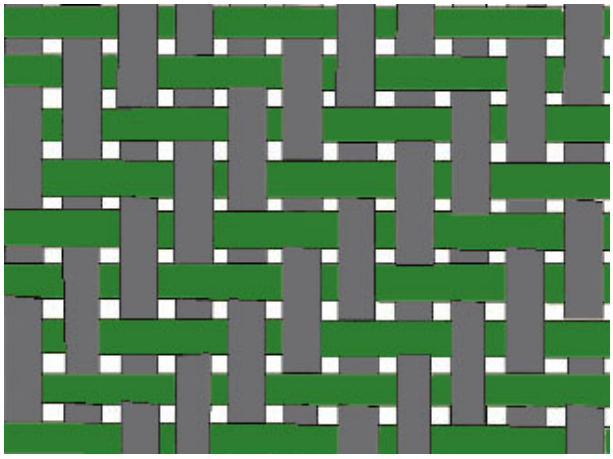

Figure 2.1: Schematic of a sheet of 2×2 twill carbon fibre fabric. Warp direction in Green, weft direction in grey.

The matrix is the Toray TC250 toughened epoxy system (neat resin density 1.21 g/cm^3) [21]. According to the datasheet, TC250 is a 130 °C cure system; after cure, it can reach a dry T_g of about 140 °C (wet T_g ≈125 °C). The recommended cure cycle includes a ramp of 1-3 °C/min, a dwell at 88±5 °C for 30-60 min, followed by a hold at 130±3 °C for at least 2 h under vacuum [21]. This resin can be free-standing post-cured to 177 °C to increase the high temperature performance (dry T_g ≈180 °C) [21].

Although the same material system is used throughout this study, laminate properties can be influenced by the curing history (Section 1.2.1). In this study, two batches that followed two distinct curing histories are considered.

- Baseline Cure (BC): curing performed according to the Technical Process Specifications (TPS) and consistent with the recommended cure cycle.
- Deviated Cure (DC): curing affected by an unintentional deviation from the specified thermal profile, resulting in a different thermal history compared to BC.

The curing cycles for both batches are described in detail in Section 2.2.1.

All samples directly tested in this thesis were extracted from the DC batch. The mechanical properties of the BC batch are taken from a certified material characterisation campaign commissioned by Persico Marine and performed by a certified laboratory. These results are used as a reference benchmark to quantify the effect of the non-conforming cure history.

Table 2.3 shows a summary of the two batches considered in this study.

Table 2.3: Investigated batch codes and summary.

Batch	TPS compliance	Source of data	Purpose in study
BC	Yes	Certified lab (Persico Marine)	Benchmark dataset for comparison
DC	No	Direct experimental testing	Experimental batch investigated in this thesis

2.2. Specimen Production

The plies were cut using a computer-controlled plotter and hand stacked according to the prescribed fibre orientation stacking sequence (later reported for each type of sample). Prepreg layup was performed in a controlled clean-room environment to minimise contamination and foreign object debris, on an open mould (table) covered with a release film to facilitate demoulding and a peel ply to obtain the required surface texture.

To improve consolidation and reduce trapped air, a debulking step was performed every three plies by vacuum bagging the layup and applying vacuum for at least 15 minutes.

After the layup was completed, the panel was prepared for autoclave curing using a standard vacuum bagging to provide compaction and evacuate trapped air and volatiles [22]. A perimeter dam was applied to limit the flow of lateral resin. A second peel ply and a high-temperature release film were placed on top of the laminate, followed by an aluminium caul plate to improve thickness uniformity. A breather/bleeder layer was applied to maintain vacuum continuity and absorb excess resin, and two vacuum ports were installed on the breather. The assembly was sealed with tacky tape and enclosed in a high-temperature vacuum bag (Figure 2.2).

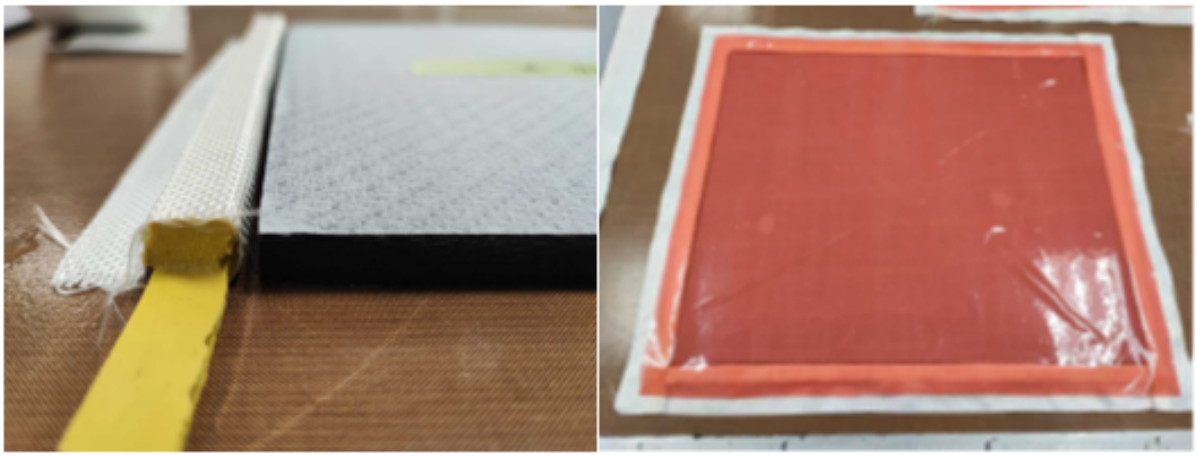

Figure 2.2: Peel-ply and dam disposition (left); release film disposition (right).

Vacuum was applied, and a vacuum drop test was performed to check for leaks. Thermocouples were attached to record the temperature during the cure. The panel was then cured in an autoclave under combined temperature, pressure, and vacuum. The details of the cure cycle are reported in Section 2.2.1.

Figure 2.3 summarises the bagging stack.

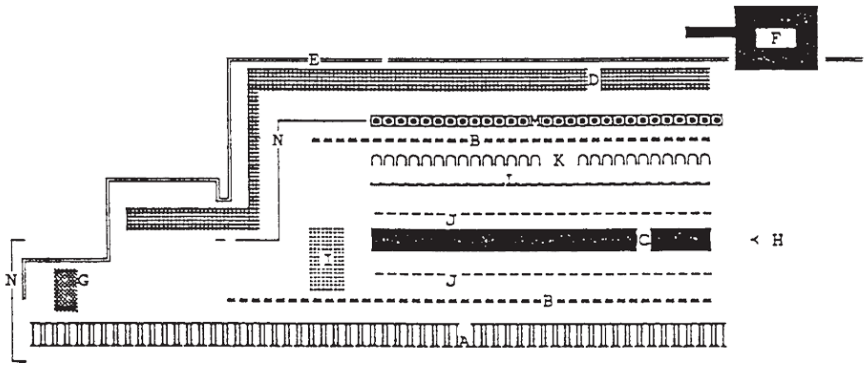

A	Base Plate	J	Peel Ply (used on panels that undergo secondary bonding
B	TFE Film	K	Bleeder cloth (may be several plies)
C	Laminate	L	Release Fabric
D	Air Breather	M	Caul Plate
E	Vacuum Bag	N	High Temperature Tape
F	Vacuum Coupling	O	Breather string (optional along non 0° edges of laminate to provide a path for volatile escape. String must contact air breather).
G	Sealant	P	25 mm (1 in.) wide bleeder cloth
H	Thermocouple		
I	Dam		

Figure 2.3: Summary of dressing and bagging.

During the curing phase, the laminate first consolidates as the resin starts to flow. Excess matrix material is removed via the breather/bleeder system, resulting in a reduction in laminate thickness. As the temperature increases, the viscosity of the resin increases as a result of the crosslinking reaction, ultimately forming a rigid, glassy matrix.

2.2.1. Curing Profiles of the Two Batches

Figure 2.4 shows the temperature–time profile of the Baseline Cure batch (BC). The cycle followed Persico Marine TPS and is consistent with the recommended cure schedule of TC250 (see Section 2.1). Specifically, the thermal cycle consisted of: heating rate of 1 °C/min, dwell at 88±5 °C for 60 min, followed by a hold at 130±3 °C for 2 h, followed by post-cure at 177±5 °C for 2 h [21].

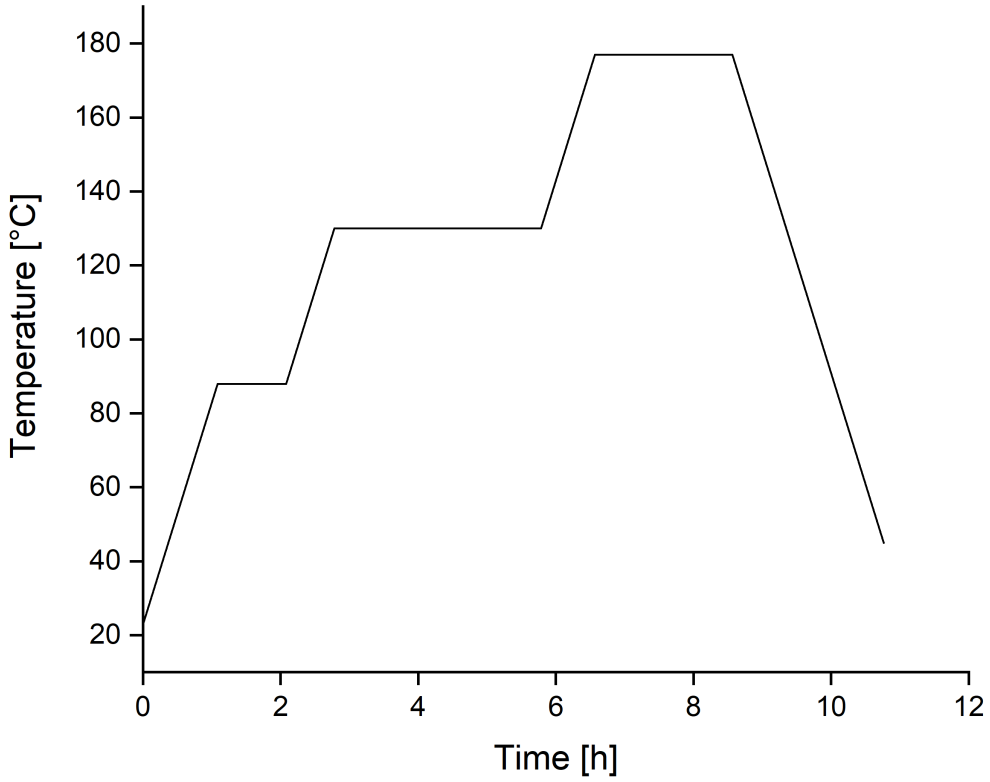

Figure 2.4: Curing cycle of BC batch.

In contrast, Figure 2.5 shows the Deviated Cure batch (DC). During the first dwell stage at 130 °C, an unexpected interruption of the autoclave occurred, resulting in an unplanned stop of the cycle. The curing was resumed several days later as an attempt to complete the process by applying the recommended temperature profile from the beginning.

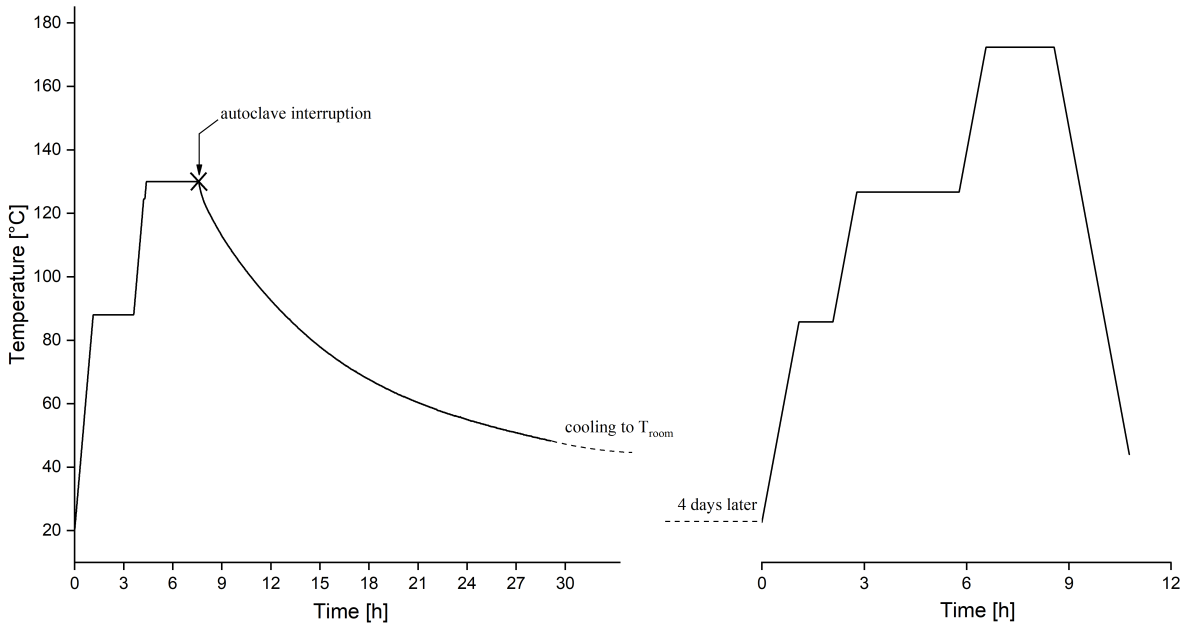

Figure 2.5: Curing cycle of DC batch.

2.2.2. Expected Effects of Cure Interruptions

For thermoset epoxies, the effect of a cure interruption depends mainly on when it occurs relative to gelation/vitrification and on whether the subsequent thermal cycle provides sufficient time and temperature to complete network formation [5, 6]. If the interruption occurs early and the resumed cycle supplies adequate thermal energy, the degree of cure and T_g may remain close to the nominal values [6]. In contrast, prolonged time at intermediate temperature and/or interruptions after gelation can reduce the achievable degree of cure and T_g, and may degrade matrix-dominated properties and interlaminar integrity [8–10].

TC250 is a toughened epoxy system formulated to handle a variety of industrial processing conditions [21]. It is therefore plausible that the Deviated Cure batch may still yield acceptable mechanical properties; however, this can only be confirmed by experimental characterisation. The following sections present the experimental analysis and quantify the effect of the DC thermal history on the thermochemical and mechanical response of the CFRP material by comparison against the Baseline Cure reference.

2.3. Test Procedures and Instrumentation

As described in Section 2.1, all samples experimentally tested in this thesis were extracted from the Deviated Cure batch (DC). Baseline Cure (BC) test results are taken from Persico Marine's Material Characterisation Campaign and used as the reference benchmark.

Thermochemical characterisation was performed to quantify the cure state and laminate quality. This included the glass transition temperature (T_g), the Coefficient of Thermal Expansion (CTE), the residual reaction enthalpy, and the constituent contents. Mechanical tests were selected for their sensitivity to matrix-dominated behaviour and are therefore suitable for detecting the effects of cure cycle deviations. The following sections provide a detailed description of each test method.

2.3.1. Differential Scanning Calorimetry (DSC)

Differential Scanning Calorimetry (DSC) was performed on (i) as-received prepreg material (uncured reference condition) and (ii) cured laminates from both batches (BC and DC). This was performed to quantify the total cure enthalpy (H_t) of the uncured reference, the residual cure enthalpy (H_r) of both batches of cured laminate, and the corresponding degree of cure (DoC). For each condition, three specimens were tested ($n = 3$).

For DC specimens, measurements were performed using a Mettler DSC-30 connected to a Mettler Toledo TC15 TA controller. The masses of the specimens were recorded with a Mettler AE163 balance (± 0.01 mg) and placed in 40 µL aluminium crucibles (ME-27331). The tests were carried out with a single heating ramp from 0 °C to 300 °C at 10 °C/min [23].

A preliminary two-ramp test was performed on one DC specimen to evaluate whether a second heating scan provided additional information. No additional reaction was detected on the second scan, and T_g could not be resolved. Subsequent measurements were therefore made using a single heating ramp.

The total cure enthalpy H_t (uncured reference) and the residual enthalpy H_r (cured laminates) were obtained by integrating the heat-flow curve (baseline-corrected) and normalising by the mass of the specimen. The degree of cure (DoC) was calculated as:

$$DoC = \frac{H_t - H_r}{H_t} \cdot 100 \tag{2.1}$$

2.3.2. Thermo Mechanical Analysis (TMA)

Thermo Mechanical Analysis (TMA) was used to measure the linear coefficient of thermal expansion (CTE) of the laminate only for the DC batch. In addition, TMA was used to estimate the T_g for the DC batch, while for the BC batch, the T_g was determined through Dynamic Mechanical Analysis by the certified lab (see Section 2.3.3). For the DC batch, direct determination of T_g through DMA measurements was not possible due to instrument limitations.

The methodology follows ASTM E831 for linear thermal expansion and ASTM E1545 for the determination of T_g by TMA [24, 25].

The tests for the DC sample were performed using a TA Instruments TMA450 in a nitrogen atmosphere to minimise oxidative effects during heating. A constant probe force of 0.05 N was applied to maintain contact without mechanical loading of the laminate. The thermal program consisted of a single linear heating ramp from 0 °C to 200 °C at 5 °C/min, consistent with the recommended practice in the referenced standards [24, 25]. The experimental setup is shown in Figure 2.6. All specimens tested were extracted from laminates with stacking sequence $[45/0]_{4s}$ where 0° denotes the warp direction. Warp and weft directions are defined as shown in Figure 2.1. The specimen geometry consisted of a length and width of 13 ± 1 mm and a thickness of 3.5 ± 0.5 mm.

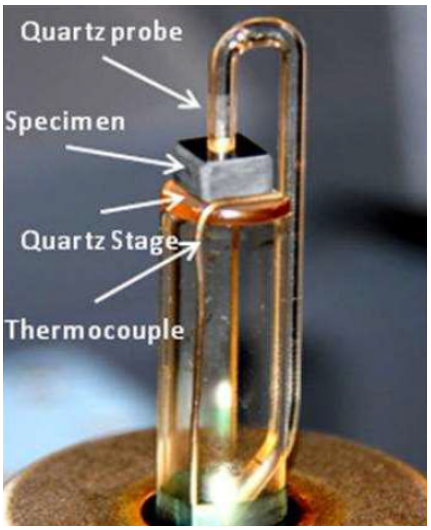

Figure 2.6: Specimen under TMA probe.

For one specimen, the measurement was repeated with a second identical heating ramp to verify the absence of transient effects between the first and second runs (e.g., settling, relaxation of residual stresses, or minor morphology changes during the first heating)

[25, 26]. Since no significant differences were observed between the two ramps, only a single ramp was used for the remaining specimens.

CTE was measured in the through-thickness direction ($n = 4$ specimens) and along one in-plane direction ($n = 4$ specimens). Only one in-plane direction was selected because the laminate (i.e., each specimen) is symmetric and balanced, so the in-plane expansion response is expected to be equivalent in the transverse and longitudinal directions (Figure 2.7) [27].

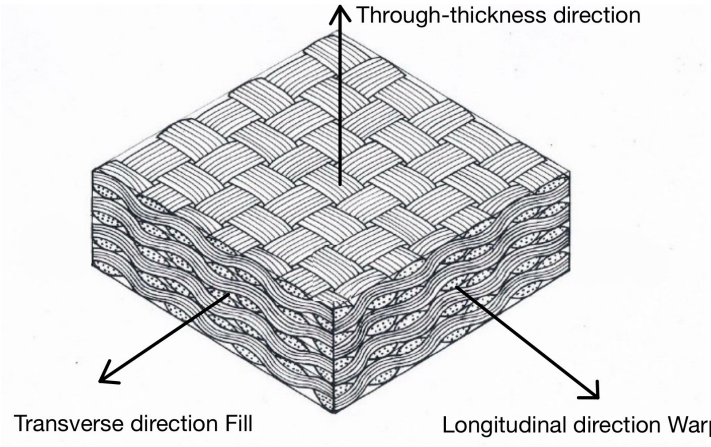

Figure 2.7: Directions of a woven fabric laminate.

From the measured dimensional change (dL/dT), the instantaneous linear thermal expansion coefficient α_T is calculated as:

$$\alpha_T = \frac{1}{L_0} \cdot \frac{dL}{dT} \tag{2.2}$$

where L_0 is the length of the specimen at the beginning of the scan. Two apparent CTE values were extracted by linear fitting of the dimension change–temperature (L–T) curve in the glassy region (α_g) and in the post-transition region (α_r), as illustrated in Figure 2.8.

The glass transition, on the other hand, appears in TMA as a distinct change in thermal expansion behaviour. Below T_g, the matrix is glassy and exhibits a lower expansion rate, whereas above T_g, increased chain mobility produces a higher expansion rate. Following standard practice, T_g was determined as the intersection of the tangents fitted to the two linear regimes of the L–T curve (Figure 2.8) [25, 28–30].

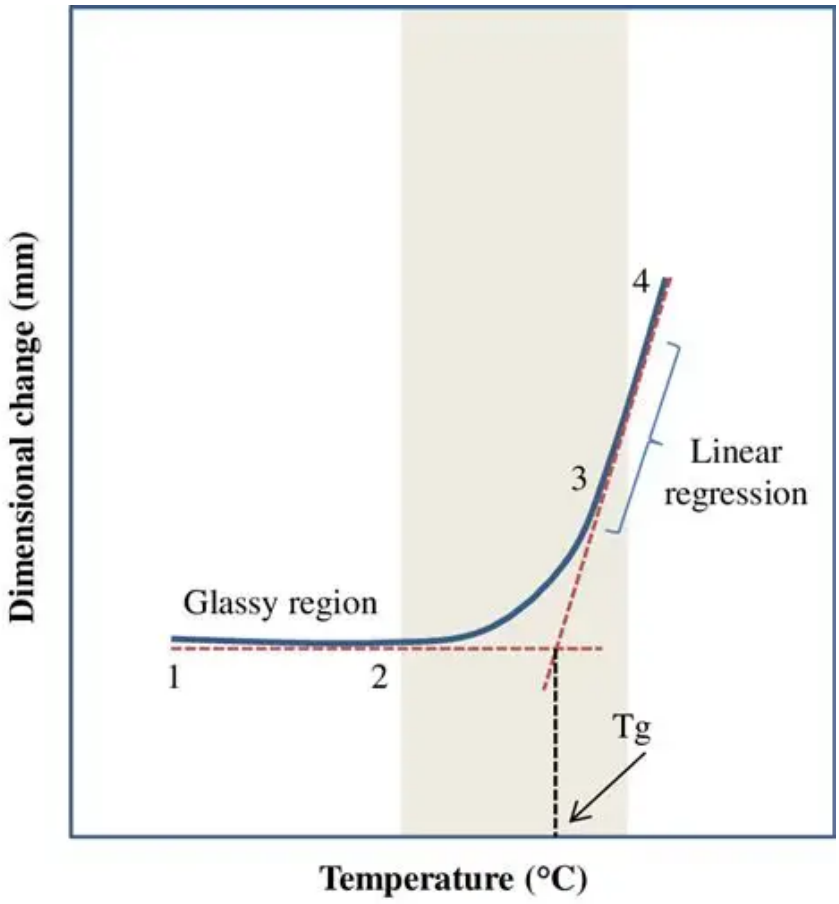

Figure 2.8: Determination of T_g Through TMA.

Finally, the T_g obtained for the DC batch by TMA was compared with the T_g measured for the BC batch by Dynamic Mechanical Analysis (DMA). DMA measurements were not available for the DC batch due to laboratory instrument limitations.

2.3.3. Dynamic Mechanical Analysis (DMA)

Dynamic Mechanical Analysis was performed by the certified lab on the Baseline Cure (BC) batch to determine its glass transition temperature. The test methodology followed ASTM D7028 [31]. Three specimens ($n = 3$) were tested. All specimens tested were extracted from laminates with stacking sequence $[45/0]_{2s}$ where 0° denotes the warp direction. The specimen geometry consisted of a length of 55 ± 1 mm, a width of 10 ± 1 mm, and a thickness of 2 ± 0.5 mm.

Measurements were carried out using a Mettler Toledo DMA1 (StarSystem) in a three-point bending configuration, with a support span of 15 mm. Because T_g measured by DMA depends on frequency and heating rate, standard test conditions were adopted [31]. The

oscillatory loading frequency was set to 1 Hz. A constant displacement amplitude of 7 μm was imposed to keep the response within the linear viscoelastic regime. The temperature program consisted of a single heating ramp from 25 °C to 300 °C at 5 °C/min, according to ASTM D7028 [31]. During scanning, the storage modulus (E'), the loss modulus (E''), and the damping factor ($\tan \delta = E''/E'$) were measured as functions of temperature.

Following ASTM D7028, T_g was determined from the storage modulus–temperature curve using the tangent intersection method on a semi-log plot of E' vs. temperature [31]. This approach is based on the marked reduction in storage modulus that occurs through the glass transition. Outside the transition region (before and after), the storage modulus is relatively constant. In this method, the DMA T_g is defined as the intersection of two tangents constructed on the storage modulus–temperature curve. A first tangent (Line A) is fitted to the pre-transition (glassy) region of $\log(E')$. A second tangent (Line B) is constructed at the inflection point to approximately the midpoint of the drop in the storage modulus. The intersection between Line A and Line B is taken as the storage modulus glass transition temperature, T_g.

Figure 2.9 shows an ideal DMA thermogram and the graphical construction of the glass transition temperature discussed.

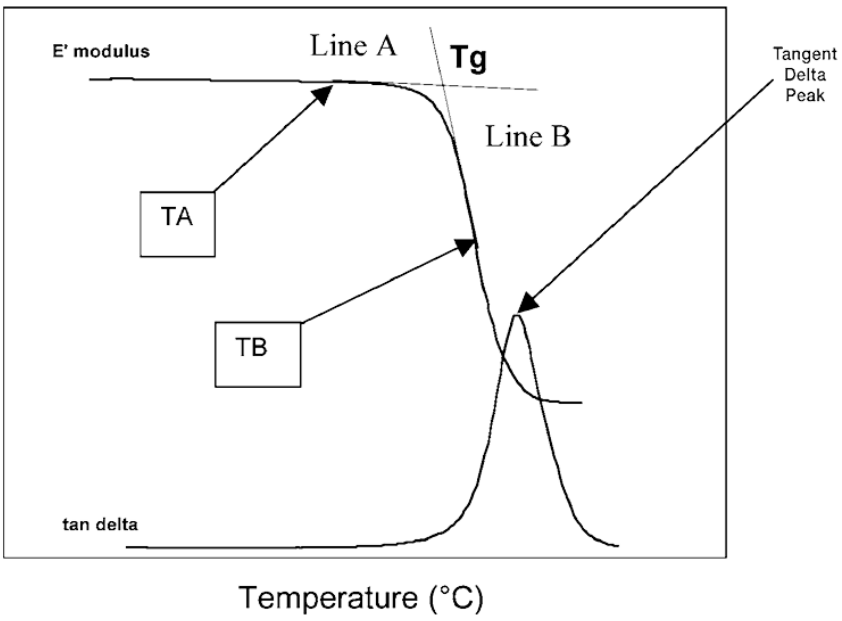

Figure 2.9: Method of detecting T_g based on the E' and $\tan \delta$ plot as a function of temperature.

2.3.4. Constituent Content Determination

Both test methods described in ASTM D3171 for the determination of the constituent content were adopted [32].

Test Method I (Matrix Digestion) :

Matrix digestion with nitric acid was used to determine the resin mass fraction of each batch (BC and DC). Three specimens were extracted from each laminate ($n = 3$ per batch) and weighed in air to obtain the initial mass M_i.

The samples were then immersed in 70% concentrated nitric acid and heated on a hot plate at 70 °C until complete dissolution of the matrix, leaving the carbon fibre reinforcement unaffected [32]. The remaining fibres were filtered, thoroughly rinsed with distilled water and acetone, then dried in an oven at 100 °C and cooled in a desiccator to minimise moisture absorption before final weighing. The dried fibre mass M_f was measured, and the resin mass fraction (resin content) was calculated from the mass loss during digestion as:

$$W_m = \frac{M_i - M_f}{M_i} \cdot 100. \tag{2.3}$$

Test method II (Thickness Based Calculation) :

This calculation was performed to determine the resin mass fraction of one panel reference, and, more importantly, the cured ply thickness (cured thickness of one ply of the prepreg system) [32].

The density of the panel ρ_c (g/cm^3) was calculated from the mass of the specimen M_i (g), its area A (m^2), and its thickness h (mm) as follows

$$\rho_c = \frac{M_i}{A\,h\,1000}, \tag{2.4}$$

the resin mass fraction was then calculated as

$$W_m = 100 - \frac{A_r\,N\,0.1}{\rho_c\,h}, \tag{2.5}$$

where A_r is the fibre areal weight (i.e., mass of one sheet of fibre per unit area, in g/m^2) and N is the number of sheets (plies) in the panel.

Finally, the cured ply thickness was calculated as

$$t = \frac{m_{pr}}{\rho_c}, \tag{2.6}$$

where m_{pr} is the prepreg areal weight (g/m^2).

2.3.5. Compression Test

Compression testing was used to determine the compressive strength, elastic modulus, and strain at failure of the two batches. Specimens were tested along the two principal in-plane directions (0° and 90°), with $n = 10$ specimens per orientation. All specimens tested were extracted from laminates with the stacking sequence $[0]_{11}$ where 0° denotes the warp direction.

The Deviated Cure (DC) specimens were tested according to ASTM D695, while the Baseline Cure (BC) reference data set was generated according to ASTM D6641.

ASTM D695 was selected due to equipment constraints, as the fixtures required for ASTM D6641 were not available in the laboratory. The validity of ASTM D695 for CFRP compression tests has been discussed in previous studies [33–35] and, as shown in Section 3.5, the results obtained in this work are consistent with the expected trends.

Compression tests were performed only at room temperature for the BC batch, while the DC batch was tested at both room temperature and high temperature ($T = 120$ °C). Table 2.4 summarises the compression test matrix.

Table 2.4: Summary of compression tests performed in this study.

Batch	**Orientations**	***n* per orientation**	**Temperature**	**ASTM**
BC	0°, 90°	10	T_{room}	D6641
DC	0°, 90°	10	T_{room}; 120 °C	D695

The detailed description provided in the remainder of this section refers exclusively to the tests performed directly on the *DC* sample (ASTM D695).

The geometry of the specimen, the corresponding support jig, and the arrangement of the fixture are illustrated in Figure 2.10, Figure 2.11, and Figure 2.12.

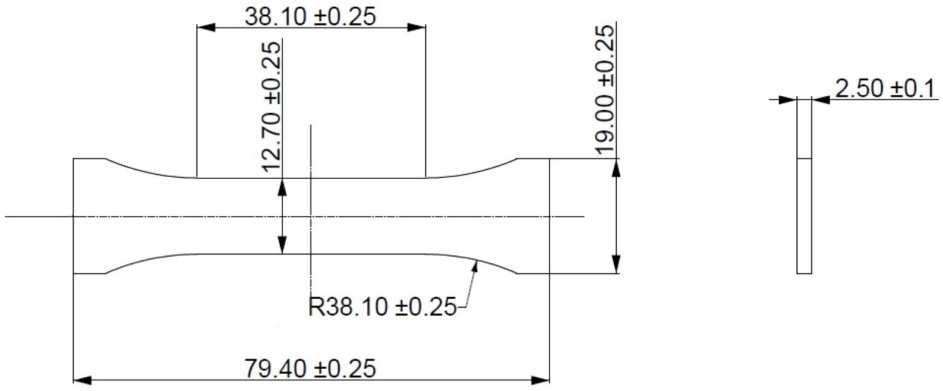

Figure 2.10: Specimen geometry of compression test ASTM D695 (mm).

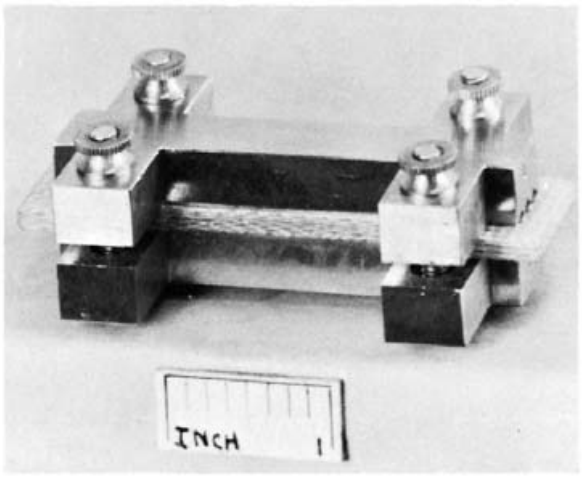

Figure 2.11: Support jig of compression test ASTM D695.

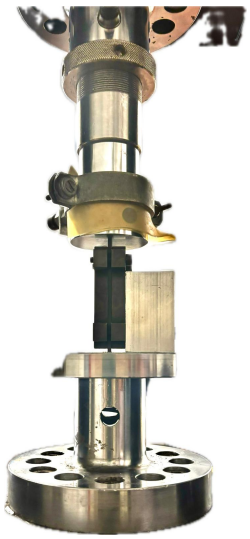

Figure 2.12: Fixture arrangement of compression test ASTM D695.

An electromechanical dynamometer (Instron 1185) equipped with a 100 kN load cell was used. The tests were carried out under displacement control at a crosshead speed of 1.3 mm/min as specified in ASTM D695 [33]. All tests were performed under standard laboratory atmospheric conditions. The load and crosshead displacement were recorded using Instron Bluehill software.

Compressive strength values were calculated based on the maximum recorded load (P_{max}) and the cross-sectional area of the specimen (A), as detailed in Equation 2.7:

$$F_{cu} = \frac{P_{\max}}{A} \tag{2.7}$$

No contact extensometer or strain gauges were used; therefore, strain values and elastic modulus were extracted from the corrected load vs. displacement response. In fact, raw crosshead displacement includes two unwanted contributions that can lead to an overestimation of strain if not corrected [36–38]. The first contribution arises from the elastic deformation of the load frame/fixtures (machine compliance), the second from seating/alignment effects of the specimen during the first stages of loading. To reduce these systematic errors, the procedure described by Gruber [37] was adopted. This double correction removes the portion of displacement that does not correspond to the specimen deformation and is essential to obtain accurate strains, particularly in stiff composite laminates.

Machine Compliance Correction :

The machine compliance correction $d_m(P)$ was modelled using a non-linear compliance function [37, 38], as shown in equation 2.8.

$$d_m(P) = KP + d_{ns}(1 - exp(-kP^b)), \tag{2.8}$$

where P is the applied load, K is the linear compliance coefficient, d_{ns} is the non-seating displacement term, and k and b are empirical parameters obtained from calibration (depending on the specific test frame and boundary conditions [37]). The trend of the latter curve is shown in Figure 2.13.

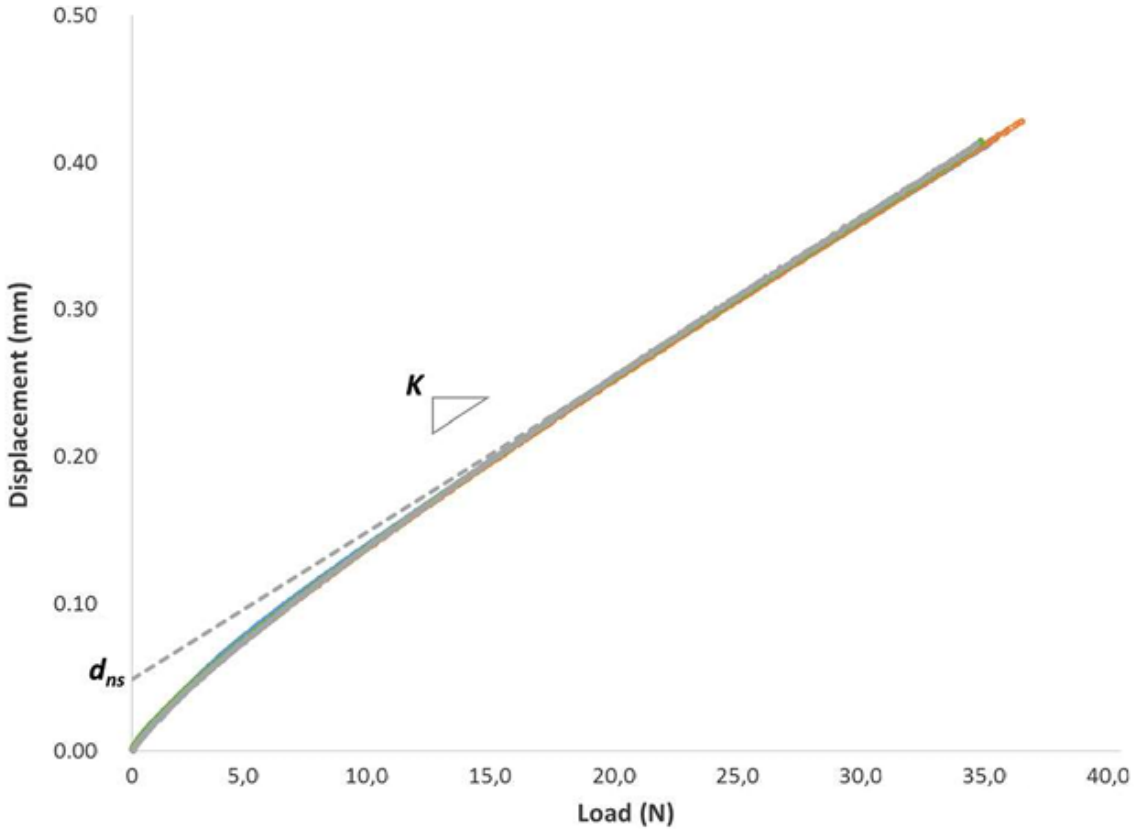

Figure 2.13: Machine displacement vs. load.

The true specimen deformation $d_s(P)$ was then obtained as shown in Equation 2.9

$$d_s(P) = d_{\text{raw}}(P) - d_m(P) \tag{2.9}$$

where d_{raw} is the measured raw crosshead displacement.

Correction for the Toe Region :

The initial portion of the specimen deformation vs. load often exhibits a toe region due to seating, fixture alignment, and specimen imperfections (Figure 2.14). To remove this effect, a straight line was fitted to the genuine linear portion of the corrected curve (CD segment in Figure 2.14) and extrapolated to intersect the zero-stress axis. The intersection point (B) was taken as the corrected zero-strain reference, and the data preceding this point were discarded. The elastic modulus and strain-to-failure were then evaluated from the corrected curve using this shifted origin [33, 37].

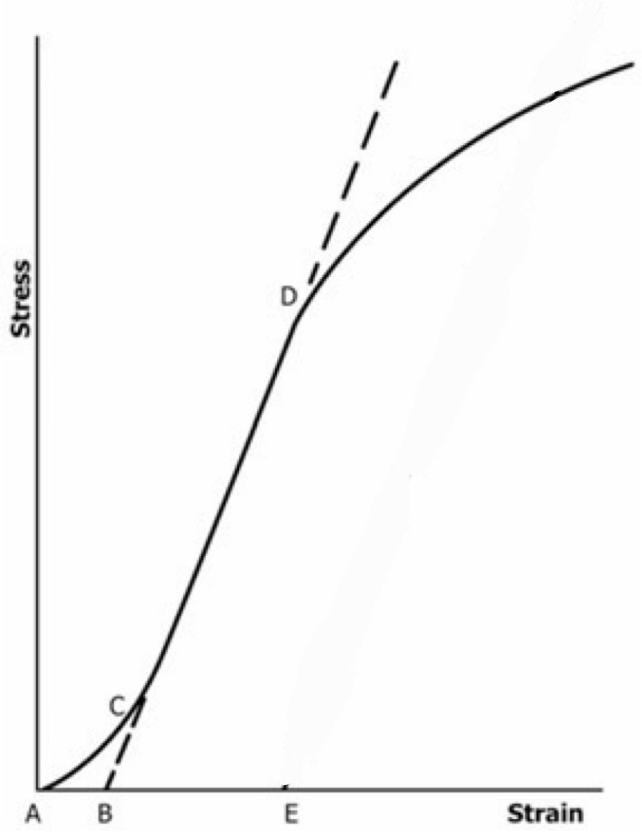

Figure 2.14: Toe region correction of the stress vs. strain curve.

Together, machine compliance correction and toe region removal improve the physical validity of the derived strain and modulus for stiff composite laminates tested without direct strain measurement. This double correction allows for the determination of the strain at failure ε_{cu} and the elastic modulus E.

2.3.6. Impact and Compression After Impact (CAI)

The effect of impact damage on the residual compressive strength of the laminates was investigated by means of low-velocity impact followed by Compression After Impact (CAI), according to ASTM D7136 (impact) and ASTM D7137 (CAI) [39, 40]. These methods provide comparative guidance on the damage tolerance of composite laminates of similar material systems, thickness, and stacking sequence; however, damage tolerance remains strongly dependent on boundary conditions, impact parameters, and the specific laminate configuration.

All specimens were manufactured with the geometry reported in Figure 2.15, with a stacking sequence $[45/0/-45/90/45/0]_s$.

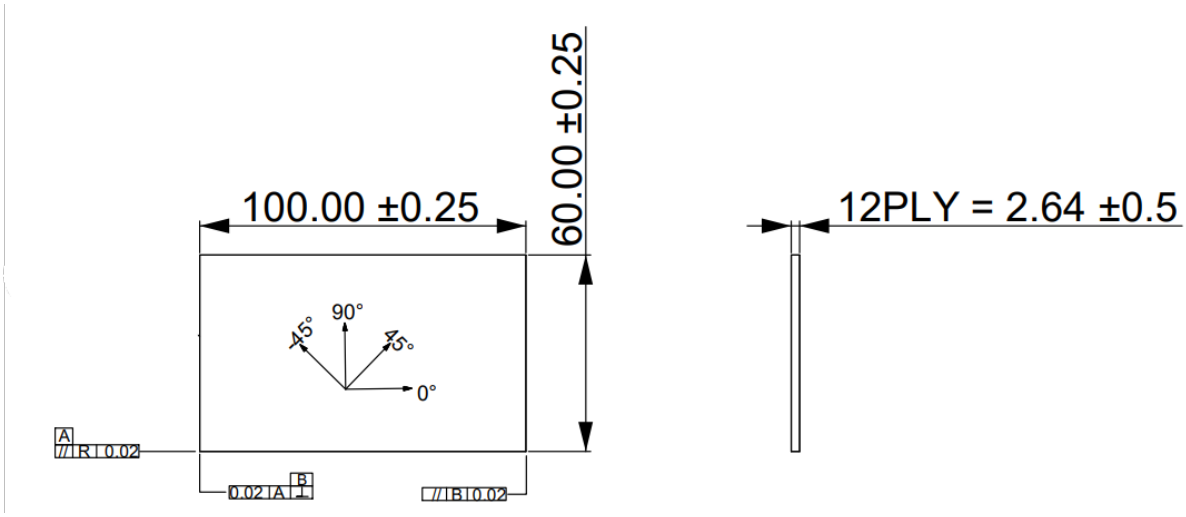

Figure 2.15: Specimen geometry of impact and CAI tests (mm).

For the DC batch 13 nominal impact energy levels were investigated, with four repetitions per energy level ($n = 4$). After impact, two specimens per energy level were tested in CAI at room temperature and two at elevated temperature (120 °C).

For the BC batch, the campaign was characterised by two representative impact energies with $n = 10$ repetitions each: BVID condition (Barely Visible Impact Damage) and a perforation condition. After impact, BC batch specimens were tested in CAI only at room temperature.

BVI and perforation conditions were also included within the 13 energy levels selected for the DC batch, allowing a direct comparison of post-impact compressive behaviour between BC and DC under matched damage severities. Specific energy values, damage metrics, and residual-strength results are reported in Section 3.6.

Table 2.5 summarises the impact test matrix.

Table 2.5: Test matrix for impact and CAI tests.

Impact Energy E_i [Joule]	BC Batch	DC batch	
	Troom	Troom	120 °C
0.0	0	3	3
4.8	0	2	2
6.7	0	2	2
9.5	10	2	2
10.5	0	2	2
14.0	0	2	2
14.7	0	2	2
15.5	0	2	2
16.3	0	2	2
17.1	0	2	2
18.0	10	2	2
20.2	0	2	2
23.5	0	2	2
26.7	0	2	2

The detailed impact and CAI procedures described below were performed directly on the DC batch specimens.

Drop-Weight Impact (ASTM D7136) :

Impacts for the DC batch were conducted using an Instron Fractovis 6789 drop weight tower connected to DAS4000 data acquisition system by Ceast. Impacts for the BC batch were conducted using Steplab DW750 drop weight tower connected to Tesa Microhite 600 data acquisition system. The impact base consists of a rectangular plate with a rectangular opening (see Figure 2.16). The specimen was positioned centrally on the opening and restrained to prevent rebound and unintended changes in boundary conditions. A rebound catcher was used to capture the impactor after the first strike, ensuring a single impact event for each specimen.

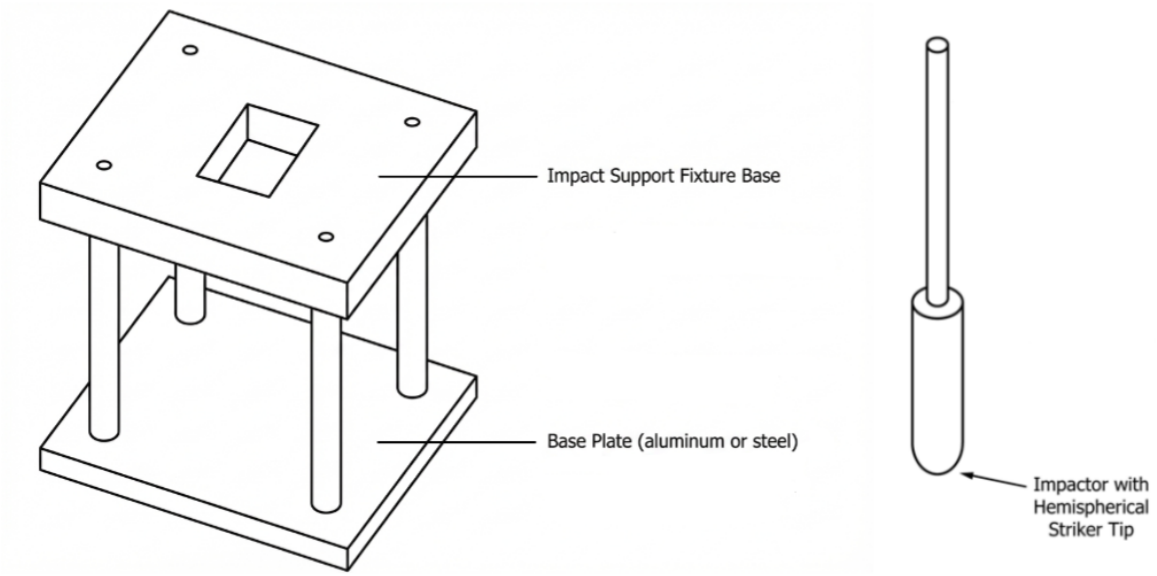

Figure 2.16: Representative rigid impact base and impactor of ASTM D7136 impact test.

Two hemispherical striker tips with diameters of 16 and 20 mm were adopted for the BC and DC batch, respectively (see Figure 2.16). The impact energy was increased by progressively increasing the impactor mass. In selected cases, the drop height (and therefore impact velocity) was also modified to reach the desired energy level. All tests were maintained in the low-velocity regime ($v < 3\,\mathrm{m/s}$).

As polymer matrix composites can exhibit rate-dependent behaviour, the potential influence of impact velocity on the viscoelastic response of the epoxy matrix is acknowledged when comparing conditions obtained via different mass/velocity combinations.

According to the standard definition, the drop height of the impactor was computed from the nominal impact energy as follows:

$$H = \frac{E_i}{mg}, \tag{2.10}$$

where E_i is the nominal impact energy (i.e., the potential energy prior to release/kinetic energy of the impactor immediately before contact), m is the mass of the impactor, and g is gravitational acceleration.

Each impact event was characterised by recording the histories of contact force–displacement (F–d), energy–time (E_a–t), and displacement–time (d–t). From the contact force–displacement response, the absorbed energy E_a was calculated as the area under the curve (Figure 2.17), defined as the total energy dissipated by the composite specimen during impact through

elastic deformation, damage formation, and frictional effects.

To evaluate the progression of damage in the composite specimens, an Energy Profile Diagram (E_a vs. E_i) was constructed using the 13 characteristic impact levels. The shape of the energy profile is governed by several factors, including the constituent materials, the architecture of the fibre and the stacking sequence, the thickness of the specimen, and the geometry of the impactor [41]. Consequently, damage mechanisms can be reconstructed by correlating the contact force–displacement response, the energy profile, and the post-impact visual inspection of the specimens [41].

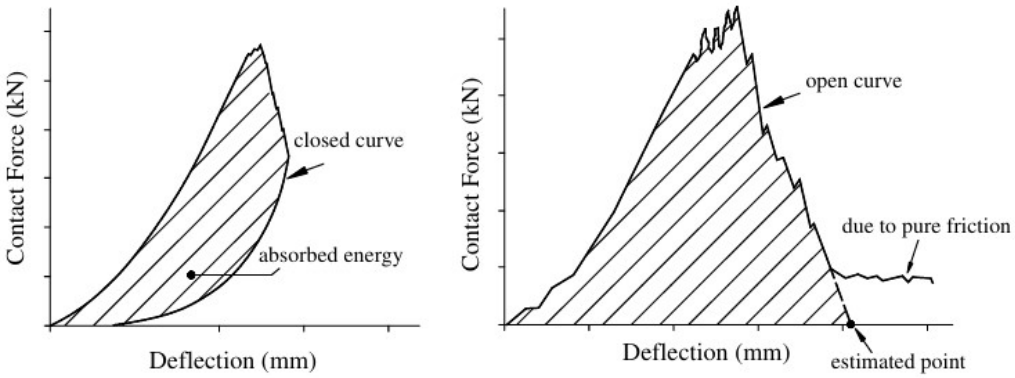

Figure 2.17: Calculation of the absorbed energy from F–d curves for a non-perforated specimen (left) and a perforated specimen (right).

As illustrated in Figure 2.17, the F–d curves can be classified as closed or open. Closed curves correspond to non-perforating impacts: after reaching a peak load, the descending branch corresponds to the elastic rebound of the impactor [41]. In contrast, open curves are associated with penetration and perforation and exhibit a characteristic horizontal "tail" at the end of the record, which is attributed to post-perforation friction as the impactor continues to move through the damaged laminate [41].

To accurately quantify the energy absorbed only by damage formation in the specimen, frictional contributions were isolated and removed when present. This correction was performed by extending the slope of the unloading (descending) branch of the F–d curve until it intersected the displacement axis, as indicated by the dashed line in Figure 2.17. The absorbed energy associated with the damage was then taken as the area under the curve up to this corrected terminal point, excluding the post-perforation frictional tail.

In addition to absorbed energy, the F–d curve was used to identify the delamination threshold force (i.e., the critical threshold force for the onset of damage, P_c). In a typical impact force history, the contact force increases until a sudden drop occurs (Point A in

Figure 2.18). This drop is associated with a rapid reduction in transverse stiffness due to the initiation of damage [42]. The force at point A can be identified as P_c [42]. The drop is then followed by partial recovery (Point B) and, in some cases, reloading (Point C) if sufficient residual kinetic energy remains in the impactor. Additional load drops may occur at higher forces as damage accumulates.

Sharp drops in the contact force response were interpreted as indicators of damage events associated with sudden reductions in local stiffness. According to ASTM D7136, oscillations in the force signal were not artificially smoothed when extracting absorbed energies and critical loads, since in composite impacts these oscillations are physically meaningful [39].

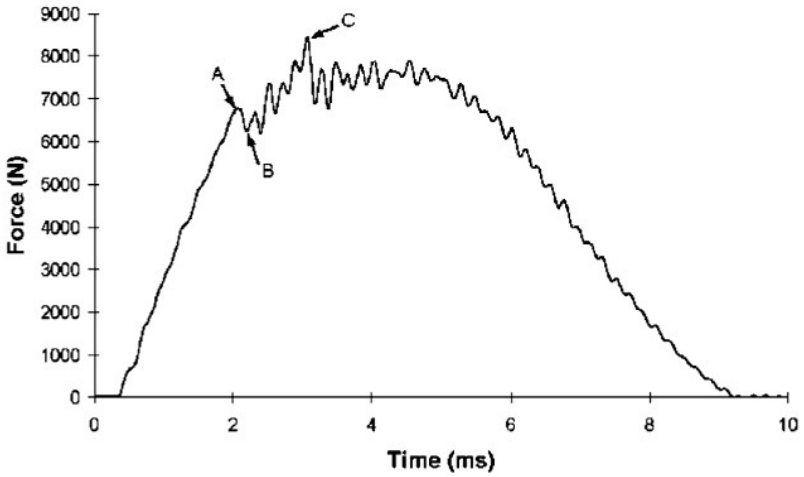

Figure 2.18: Typical impact force history showing the first load drop associated with damage initiation.

Compression After Impact (ASTM D7137) :

CAI tests were performed on impacted specimens using an antibuckling stabilisation fixture designed to suppress global buckling and minimise parasitic bending during end-loading (see Figure 2.19). Specimens were installed with the machined ends flush with the ends of the fixture, thereby centering the impact-damaged region within the fixture. Alignment was performed to ensure that the specimen was held perpendicular to the fixture base and uniformly supported by the fixture components.

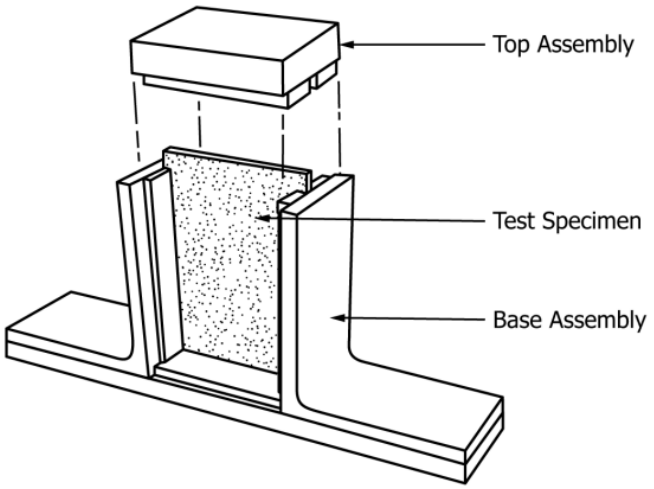

Figure 2.19: Support fixture of CAI test with specimen in place ASTM D7137.

Compression testing was carried out using an electromechanical dynamometer (Instron 1185) equipped with a 100 kN load cell. The tests were carried out under displacement control at a crosshead speed of 1.3 mm/min. The load and crosshead displacement were recorded using Instron Bluehill software.

The failure mode and the failure location were documented for each specimen according to the standard's criteria for acceptable and unacceptable CAI failures.

The ultimate compressive residual strength was calculated as

$$F_{CAI} = \frac{P_{max}}{A}, \tag{2.11}$$

where $P_{\max}$ is the maximum force carried prior to failure and A is specimen's cross sectional area.

3 | Experimental Results

3.1. Differential Scanning Calorimetry (DSC)

The DSC thermograms for the DC batch are shown in Figure 3.1. For the uncured reference and the BC batch, the corresponding graphical profiles were unavailable; therefore, only their numerical results are presented in this section.

Tables 3.1–3.3 summarise the DSC results for all conditions.

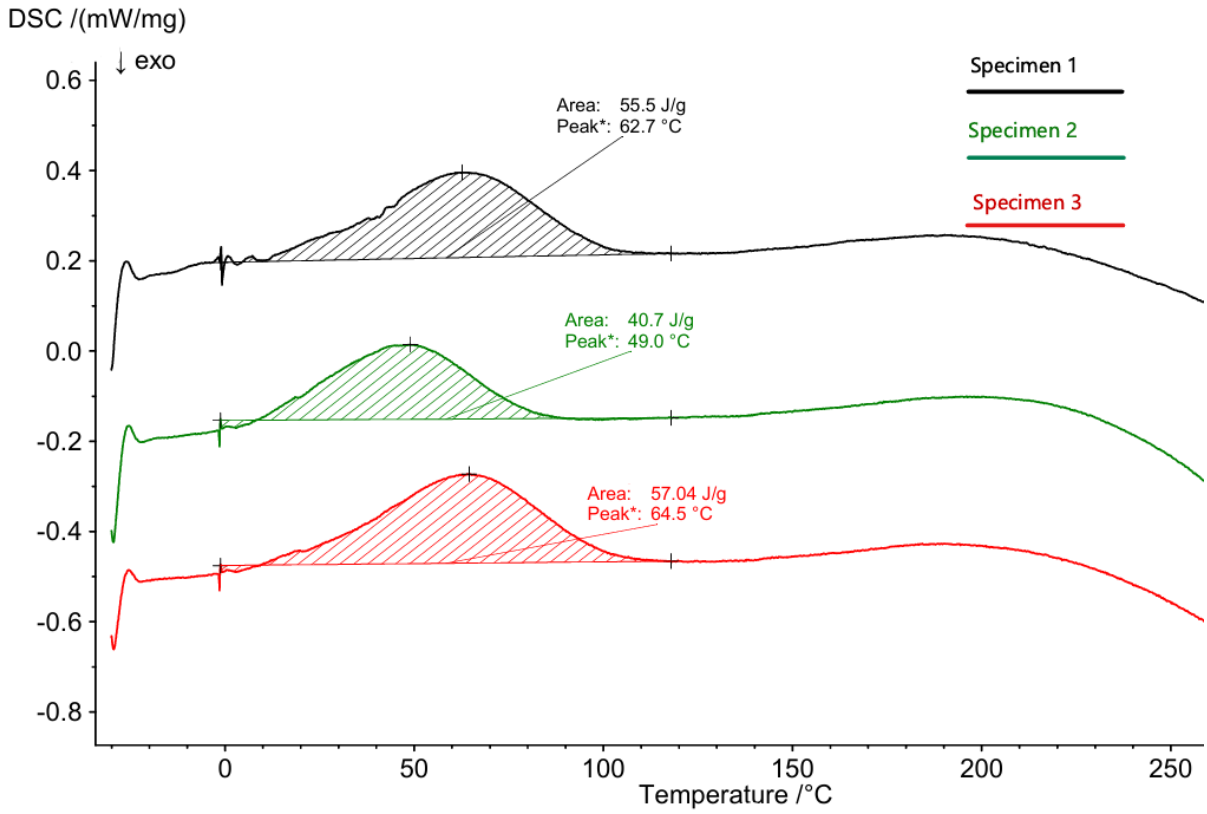

Figure 3.1: DSC thermograms for the DC batch.

Table 3.1: DSC results for uncured reference.

Specimen	H_t [J/g]	T_{peak} [°C]	T_{onset} [°C]
1	381.5	154.0	144.8
2	358.8	153.8	144.4
3	373.4	154.1	144.7
Mean	**371.2**	**153.9**	**144.6**

Table 3.2: DSC results for the Baseline Cure (BC) batch.

Specimen	H_r [J/g]	Degree of cure [%]
1	9.92	97
2	9.14	98
3	8.25	98
Mean	**9.10**	**98**

Table 3.3: DSC results for the Deviated Cure (DC) batch.

Specimen	H_r [J/g]	Degree of cure [%]
1	55.50	85
2	40.70	89
3	57.04	85
Mean	**51.08**	**86**

Because the reference condition is as-received prepreg, H_t represents an internal reference enthalpy for this material system rather than an absolute enthalpy of a fully unreacted formulation; nevertheless, it is suitable for comparing BC and DC consistently.

The uncured reference sample exhibited consistent onset and peak temperatures with a mean total reaction enthalpy of $H_t = 371.2$ J/g, which was adopted as the reference value for subsequent calculations (Table 3.1).

The BC batch showed a small residual exotherm, with a mean residual enthalpy $H_r = 9.10$ J/g, corresponding to $DoC \approx 98\%$ (Table 3.2). This indicates that the baseline cure cycle achieved a near-complete cure, leaving only a limited residual reaction potential.

In contrast, the DC batch exhibited a substantially higher residual enthalpy, $H_r = 51.08$ J/g, corresponding to $DoC \approx 86\%$ (Table 3.3). This indicates that the deviated cure cycle did not achieve a complete cure, leaving a significant residual reaction potential.

The residual enthalpy in DC is approximately 5–6 times higher than in BC (51.08 vs. 9.10 J/g), resulting in an approximately 12% reduction in the degree of cure (DoC).

3.2. Thermo Mechanical Analysis (TMA)

The thermal expansion behaviour and dimensional change of the specimens under TMA testing are illustrated in the following figures. They report the dimension change as a function of temperature for both the in-plane direction (Figures 3.3) and the through-thickness direction (Figures 3.2), highlighting the anisotropic response of the material and the characteristic slope change at the glass transition temperature (T_g).

The numerical results extracted from the TMA curves are summarised in Table 3.4, providing a quantitative comparison of the expansion coefficients in both glassy state (α_g) and rubbery state (α_r).

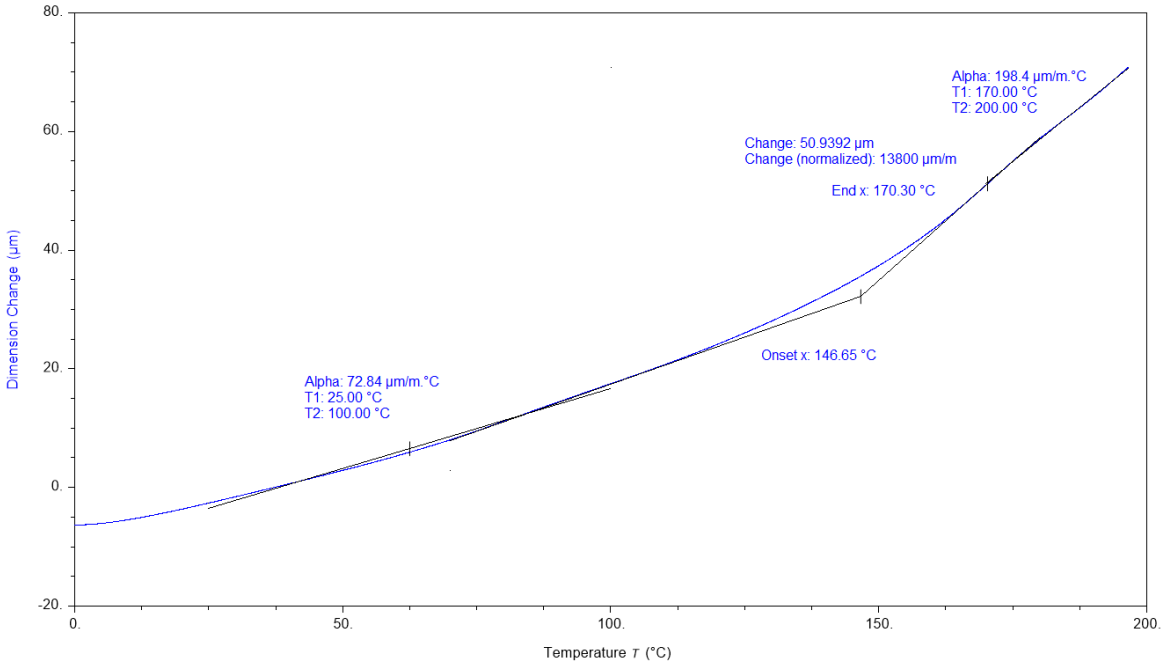

(a) Specimen 1 - Through-thickness.

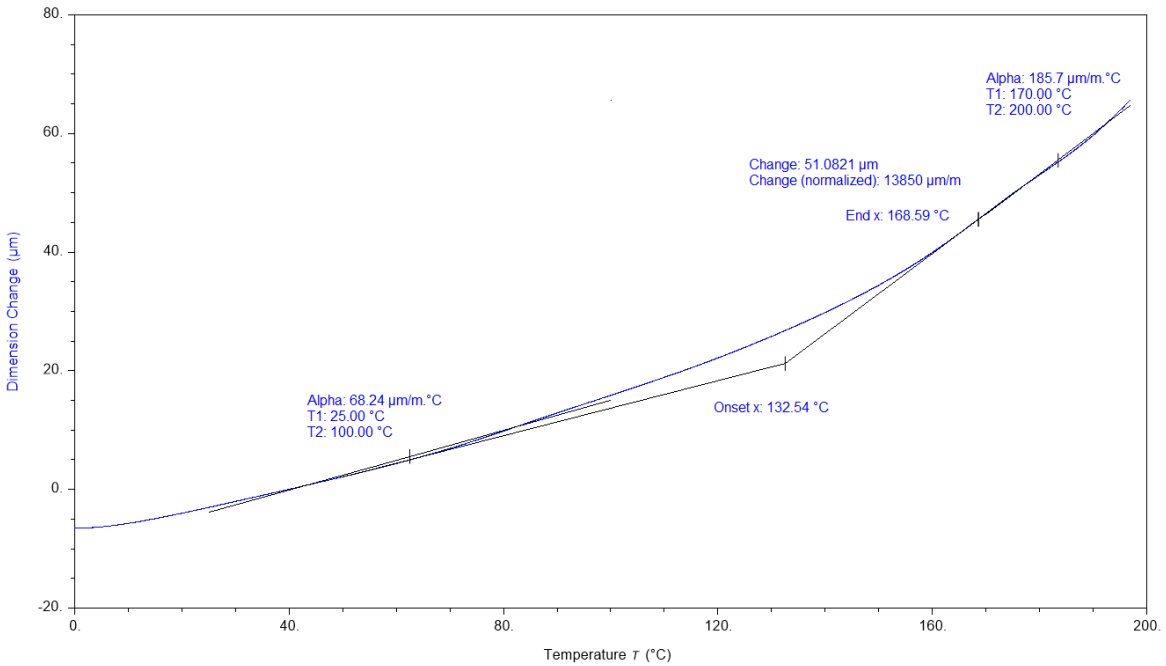

(b) Specimen 2 - Through-thickness.

Figure 3.2: Dimension change vs. temperature profiles in the through-thickness direction (part I).

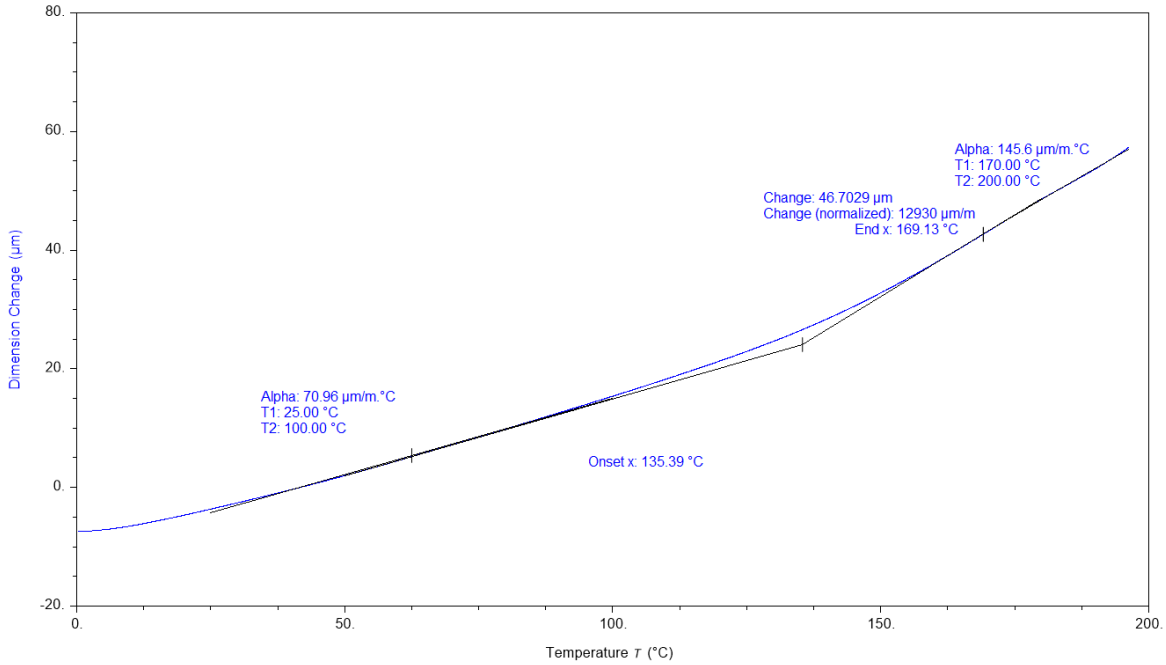

(c) Specimen 3 - Through-thickness.

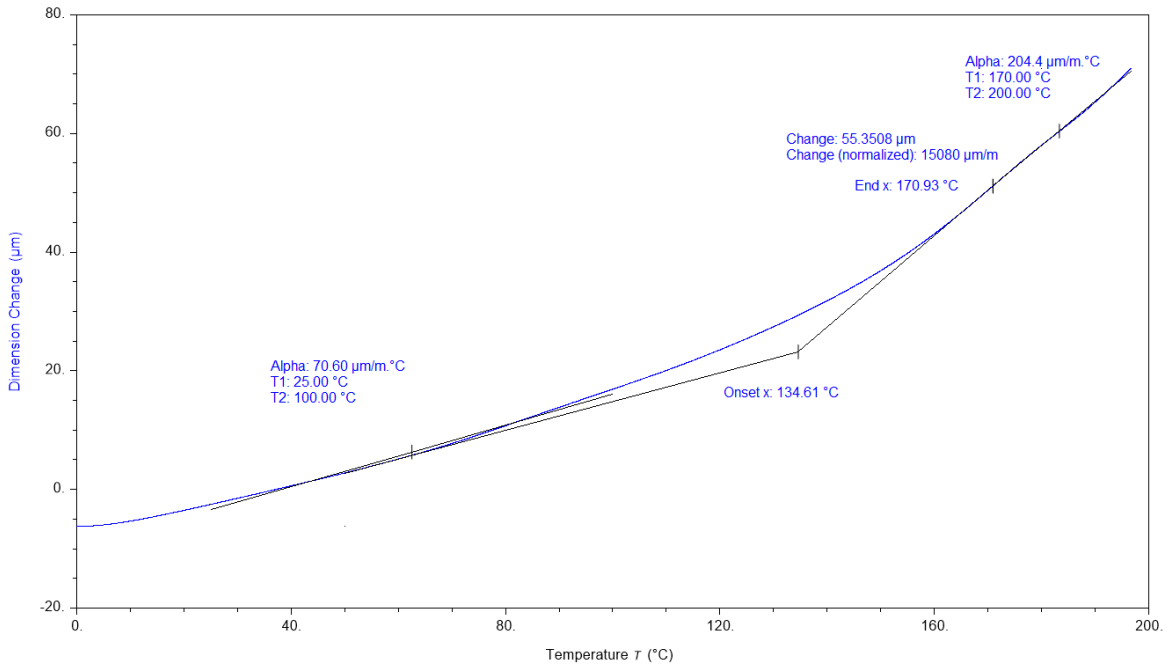

(d) Specimen 4 - Through-thickness.

Figure 3.2: Dimension change vs. temperature profiles in the through-thickness direction (part II).

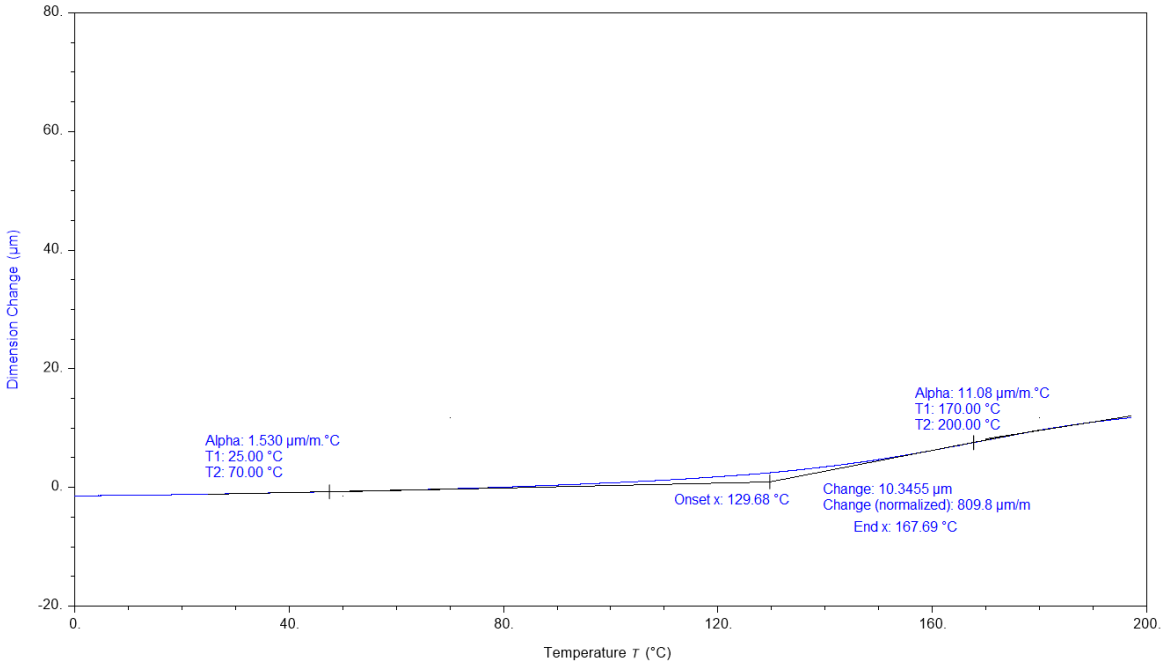

(e) Specimen 5 - In-plane.

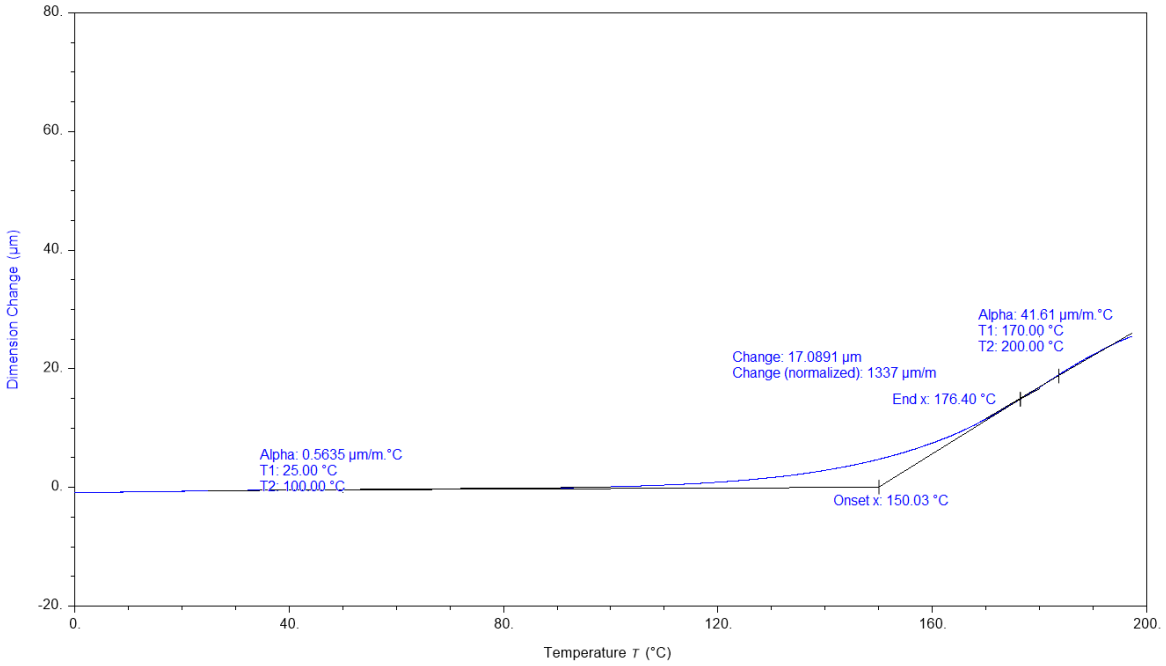

(f) Specimen 6 - In-plane.

Figure 3.3: Dimension change vs. temperature profiles in the in-plane direction (part I).

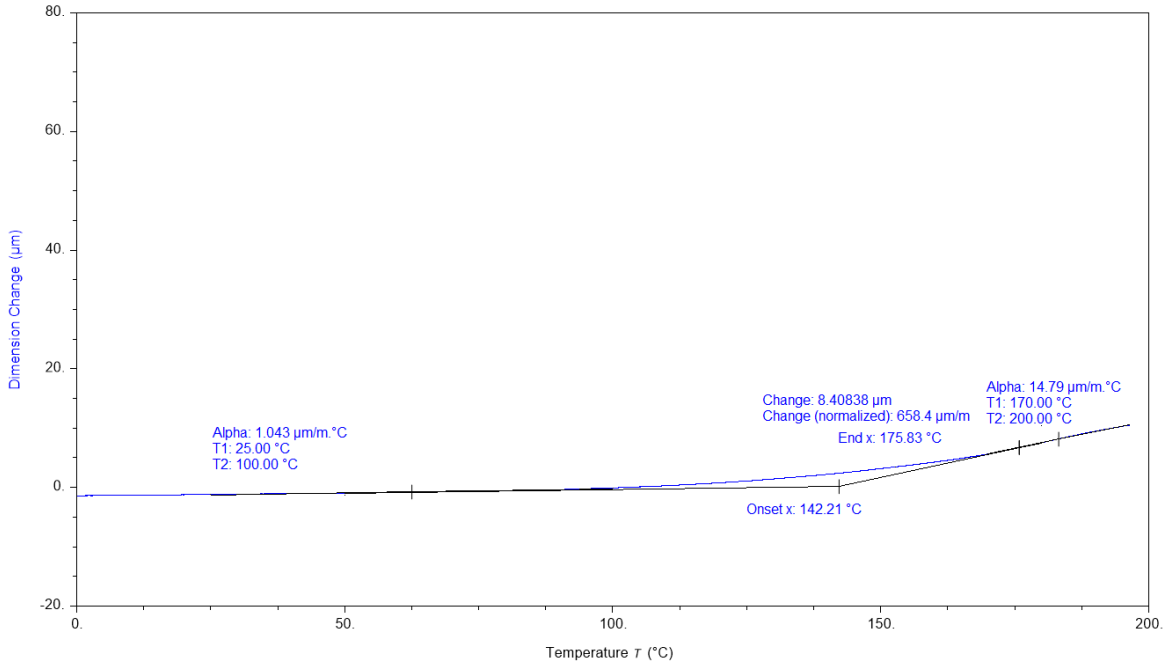

(g) Specimen 7 - In-plane.

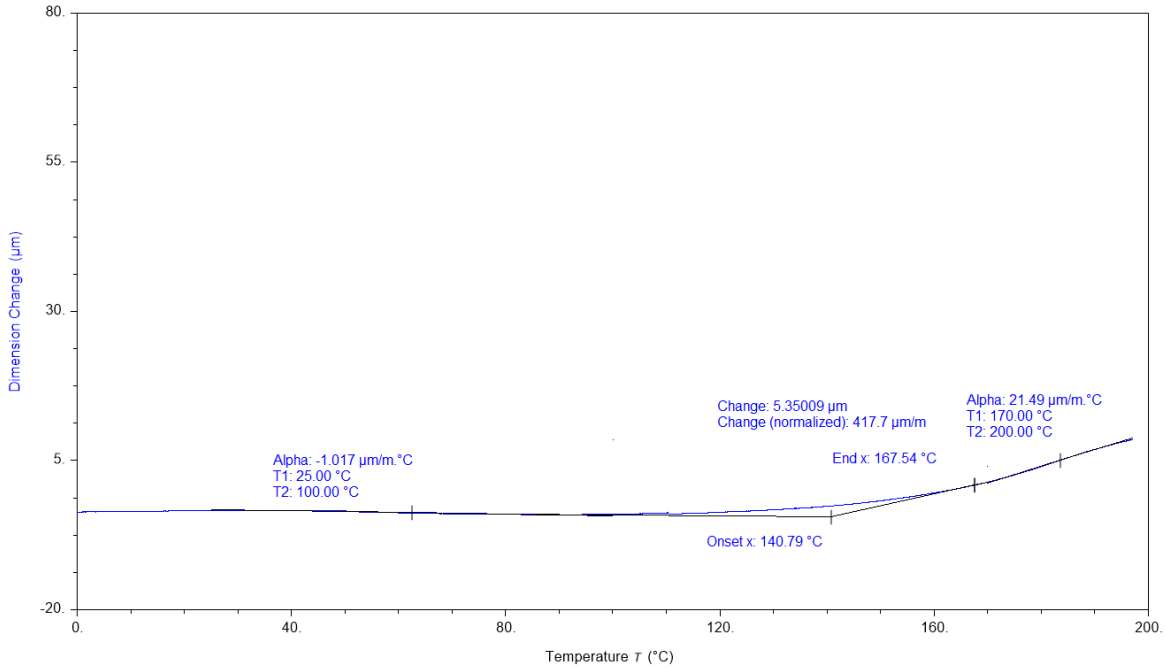

(h) Specimen 8 - In-plane.

Figure 3.3: Dimension change vs. temperature profiles in the in-plane direction (part II).

Table 3.4: Coefficients of Thermal Expansion (CTE) for through-thickness and in-plane directions.

Direction	Specimen	α_g $(T < T_g)$ $[10^{-6}\,°C^{-1}]$	α_r $(T > T_g)$ $[10^{-6}\,°C^{-1}]$
Through-thickness	1	72.84	198.4
	2	68.24	185.7
	3	70.96	145.6
	4	70.6	204.4
In-plane	5	1.53	11.08
	6	0.5635	41.61
	7	1.043	14.79
	8	-1.017	21.49

In the through-thickness direction (specimens 1–4), the material exhibits high expansion coefficients, with α_g around $70 \times 10^{-6}\ °C^{-1}$. In contrast, the in-plane CTE below T_g is close to zero or even slightly negative (specimens 5–8).

This trend is consistent with the anisotropic behaviour of the CFRP analysed. In fact, the through-thickness response is matrix-dominated: there are no continuous fibres oriented in the thickness direction to restrain the natural expansion of the epoxy resin. In contrast, the in-plane response reflects the constraining effect of the reinforcement. In fact, carbon fibres have low negative CTE in the axial direction and large positive CTE in the radial direction [27]; consequently, they suppress the thermal expansion of the matrix in the in-plane direction.

Above T_g, a clear increase in CTE is observed in both directions, consistent with the transition of the polymer matrix from the glassy to the rubbery state. In the through-thickness direction α_r reaches values up to $204.4 \times 10^{-6}\ °C^{-1}$, while in the in-plane direction α_r reaches values up to $41.61 \times 10^{-6}\ °C^{-1}$. Specifically, once T_g is exceeded, the epoxy gains mobility (higher free volume) and the thermal expansion rate increases accordingly. A similar increase, though less pronounced, is observed in in-plane direction, where fibre constraint remains dominant even above T_g.

Moreover, the CTE values in both the in-plane and through-thickness directions exhibit considerable scatter. These results demonstrate excellent agreement with the literature, with values within the same order of magnitude as those reported by other studies [27, 43].

The glass transition temperatures (T_g) of the DC batch measured by TMA are reported in Table 3.5.

Table 3.5: T_g by TMA for DC batch.

Specimen	$\boldsymbol{T_g}$ **[°C]**
1	146.7
2	132.5
3	135.4
4	134.6
5	129.7
6	150
7	142.2
8	140.8
Mean	**139**
Standard Deviation	**7.1**

The DC batch exhibits a low T_g, with significant scatter ($T_g = 139 \pm 7.1\,°\text{C}$).

Absolute T_g values are consistent with the TC250 datasheet: a dry T_g of about 140 °C is expected after standard 130 °C cure [21].

3.3. Dynamic Mechanical Analysis (DMA)

The glass transition temperatures (T_g) of the BC batch measured by DMA are reported in Table 3.6.

Table 3.6: T_g by DMA for BC batch.

Specimen	T_g [°C]
1	181.0
2	181.9
3	180.7
4	177.9
5	179.0
6	184.7
Mean	**180.9**
Standard Deviation	**2.2**

The BC batch shows a high T_g with limited scatter ($T_g = 180.9 \pm 2.2\,°C$).

Absolute T_g values are consistent with the TC250 datasheet: a dry T_g of about 180 °C is associated with an elevated temperature post-cure (i.e., 177 °C) [21].

3.4. Constituent Content Determination

Tables 3.7, 3.8 and 3.9 show the results of the two methods. The resin content is expressed in weight percentage.

Table 3.7: Results of ASTM D3171 Test Method I for the BC batch.

Specimen	Resin Content [$wt\%$]
1	38.5
2	38.9
3	38.7
Mean	**38.7**

Table 3.8: Results of ASTM D3171 Test Method I for the DC batch.

Specimen	Resin Content [$wt\%$]
1	35
2	39.8
3	39.7
Mean	**38.2**

Table 3.9: Results of ASTM D3171 Test Method II for the panel reference.

	A_r [g/m^2]	m_{pr} [g/m^2]	Resin Content [$wt\%$]
Panel Reference	197.3	331.5	40.4

For the BC batch, the resin content values are grouped between 38.5 and 38.9 wt%, with a mean of 38.7 wt% (Table 3.7). The Deviated Cure batch shows a similar mean value of 38.2 wt% (Table 3.8), with high scatter driven by one low result (35 wt%). The difference between the two batch means is small (0.5 wt%), and they both fall within the nominal resin content range reported for the prepreg system (40 ± 3 wt%) [21].

As reported in Table 3.8, one low result drives the high scatter of the results of ASTM D3171 Test Method I. In fact, for this test, incomplete digestion and/or incomplete drying increase the measured fibre mass M_f and therefore bias the calculated resin content to lower values. Fibre loss during filtration and rinsing reduces M_f and biases the resin content upward. In this case, the low resin content result for DC specimen 1 is attributed to incomplete digestion, which can also be seen by visual inspection of the recovered fibres (Figure 3.4).

Figure 3.4: Dry fibres obtained from the matrix digestion test.

Test Method II applied to the panel reference yields a resin content of 40.4 wt% (Table 3.9), close to the nominal resin content of the prepreg system.

Additionally, with Test Method II, the nominal cured ply thickness can be obtained from the ratio of the prepreg weight to the density of the panel (see Section 2.3.4), which is calculated as:

$$t = \frac{m_{pr}}{\rho_c} = \frac{331.5 \text{ g/m}^2}{1500 \text{ kg/m}^3} = 0.22 \text{ mm}. \tag{3.1}$$

This parameter is useful for design purposes, as it provides a first estimate of the number of plies required to achieve a target laminate thickness.

3.5. Compression Test

Room Temperature Tests Results :

Tables 3.10–3.13 show the room temperature compression results for the Baseline Cure and Deviated Cure batches. Direct comparison of absolute values between BC and DC must be interpreted with care because the batches were tested using different standards (BC: ASTM D6641; DC: ASTM D695). Figures 3.5 and 3.6 display the stress vs. strain curves for both orientations of the DC batch.

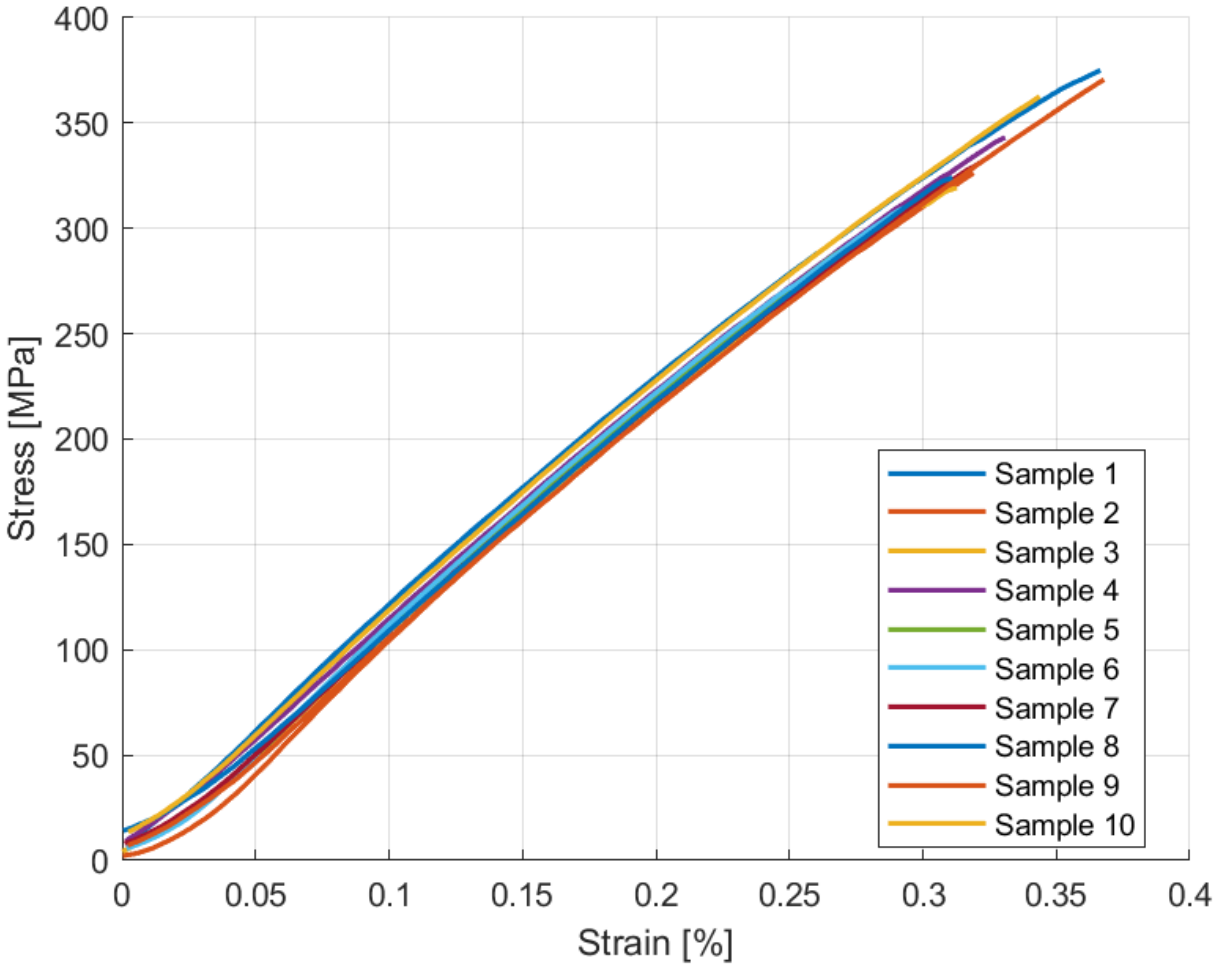

Figure 3.5: Room temperature stress vs. strain curves for 0° orientation DC batch (ASTM D695).

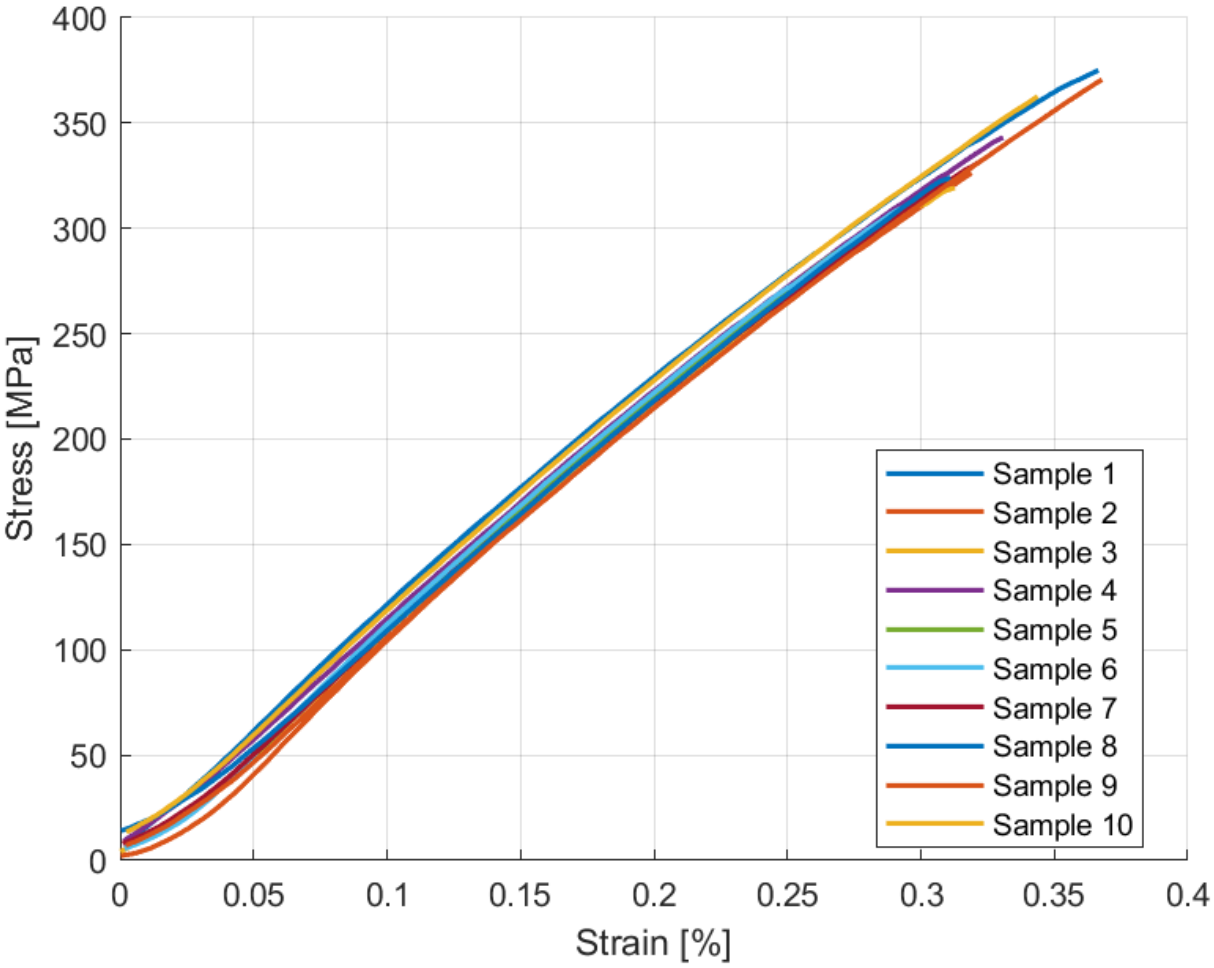

Figure 3.6: Room temperature stress vs. strain curves for 90° orientation DC batch (ASTM D695).

Table 3.10: BC batch results, 0° orientation (ASTM D6641), T_{room}.

Specimen	F_{cu} [MPa]	ε_{cu} [%]	E [GPa]
1	348	0.33	108
2	340	0.29	113
3	338	0.32	107
4	350	0.34	107
5	337	0.27	116
6	344	0.29	117
7	348	0.29	114
8	348	0.33	112
9	342	0.30	108
10	376	0.29	121
Mean	**347**	**0.31**	**112**
Standard Deviation	**11.14**	**0.02**	**4.81**

Table 3.11: BC batch results, 90° orientation (ASTM D6641), T_{room}.

Specimen	F_{cu} [MPa]	ε_{cu} [%]	E [GPa]
1	318	0.34	99
2	337	0.37	90.6
3	375	0.39	100
4	327	0.36	97
5	342	0.35	101
6	359	0.40	94
7	348	0.34	105
8	334	0.41	88
9	334	0.39	89
10	343	0.34	106
Mean	**342**	**0.37**	**97**
Standard Deviation	**16.22**	**0.03**	**6.36**

Table 3.12: DC batch results, 0° orientation (ASTM D695), T_{room}.

Specimen	F_{cu} [MPa]	ε_{cu} [%]	E [GPa]
1	375	0.37	123
2	326	0.32	108
3	319	0.31	109
4	343	0.33	115
5	320	0.31	111
6	310	0.29	112
7	333	0.32	110
8	324	0.31	110
9	371	0.37	108
10	363	0.34	119
Mean	**338**	**0.33**	**112**
Standard Deviation	**23.35**	**0.03**	**5.08**

Table 3.13: DC batch results, 90° orientation (ASTM D695), T_{room}.

Specimen	F_{cu} [MPa]	ε_{cu} [%]	E [GPa]
1	374	0.35	128
2	341	0.31	125
3	317	0.30	110
4	297	0.28	108
5	344	0.32	122
6	356	0.33	128
7	348	0.33	124
8	326	0.30	124
9	339	0.34	104
10	301	0.27	120
Mean	**334**	**0.31**	**119**
Standard Deviation	**24.14**	**0.02**	**8.73**

The BC batch exhibits a stable response in 0° orientation, with a mean compressive strength (F_{cu}) of 347 ± 11.14 MPa and an elastic modulus (E) of 112 ± 4.81 GPa. In the 90° orientation, the BC sample shows a slight reduction in the mean strength to 342 ± 16.22 MPa and a more pronounced decrease in stiffness, with a mean modulus of 97 ± 6.36 GPa. Although scatter remains limited for most parameters, the strength distribution in 90° orientation is influenced by specimen 3 (375 MPa), contributing to a higher standard deviation compared to the longitudinal direction.

For the DC batch, the mean compressive strengths are comparable in magnitude to the BC batch, calculated at 338±23.35 MPa and 334±24.14 MPa for the 0° and 90° orientations, respectively. However, a significant increase in data scatter is observed, with standard deviations for the strength nearly doubling relative to the BC batch.

The DC elastic modulus does not show a systematic reduction relative to BC.

Although a 2×2 twill fabric is expected to have a comparable in-plane response in the two principal directions, small differences can arise from weave-induced warp/weft asymmetry (e.g., crimp), and from systematic differences between sample sets.

$T = 120$ °C Tests Results :

Tables 3.14 and 3.15 show the results of the compression strength at high temperature (T = 120 °C) for the DC batch.

Table 3.14: DC batch results, 0° orientation (ASTM D695), $T = 120$ °C.

Specimen	F_{cu} [MPa]
1	266
2	285
3	279
4	244
5	263
6	255
7	254
8	281
9	297
10	280
Mean	**270**
Standard Deviation	**16.56**

Table 3.15: DC batch results, 90° orientation (ASTM D695), $T = 120$ °C.

Specimen	F_{cu} [MPa]
1	249
2	311
3	308
4	324
5	335
6	305
7	284
8	282
9	320
10	319
Mean	**304**
Standard Deviation	**25.48**

In both orientations, the compressive strengths measured at 120 °C are lower than the corresponding room temperature values, consistent with earlier studies on CFRP mechanical degradation at elevated temperature [44–47].

In the 0° direction, the mean compressive strength was found to be 270±16.56 MPa. This data set exhibits moderate statistical dispersion, with individual values ranging from a minimum of 244 MPa (specimen 4) to a maximum of 297 MPa (specimen 9). In contrast, the transverse (90°) orientation yielded a higher mean strength of 304 ± 25.48 MPa. Despite the higher average performance in the 90° set, the results show a more pronounced scatter, characterised by a standard deviation of 25.48 MPa. This increased dispersion is influenced by the lower bound result of specimen 1 (249 MPa).

The mean strength in the 90° direction is higher than in the 0° direction (304 vs. 270 MPa).

As explained earlier, for a balanced 2×2 twill fabric, comparable in-plane behaviour would be expected in the absence of systematic effects. The difference is therefore attributed to the variability between samples, and to the sensitivity of the ASTM D695 end-loaded test to alignment, seating, and end effects, which can become more critical at elevated temperature.

Only compressive strength is discussed here, as the literature indicates that elevated-temperature degradation is typically more pronounced in strength than in elastic modulus for CFRP laminates [46, 47].

Fracture Analysis :

Figure 3.7 displays the compression fracture surfaces for representative specimens at room temperature and high temperature.

Fracture surface observations indicate that the compressive failure morphology of the laminates changes with the thermal environment. The observed trends are consistent with the mechanisms and morphologies reported in the literature for fibre reinforced polymer composites [46, 47].

At both room temperature and 120°C, the compression sample exhibited a brittle macroscopic fracture. At room temperature, the fracture surfaces showed clear evidence of matrix damage and fibre shear fracture; in addition, significant delamination was visible across plies. The fracture surface was approximately an oblique line (45°).

In the high-temperature condition, failure was triggered by resin softening due to the glass transition process, which caused a kinking-type fracture. These failure mechanisms are caused by the softening of the resin that no longer confines the fibres, and eventually,

such a lack of lateral stability leads to fibres buckling. The fracture line became more irregular and uneven compared to the room-temperature case, and several fibres showed visible inclination and local buckling. Delamination was still present but appeared less pronounced than in the room-temperature coupons.

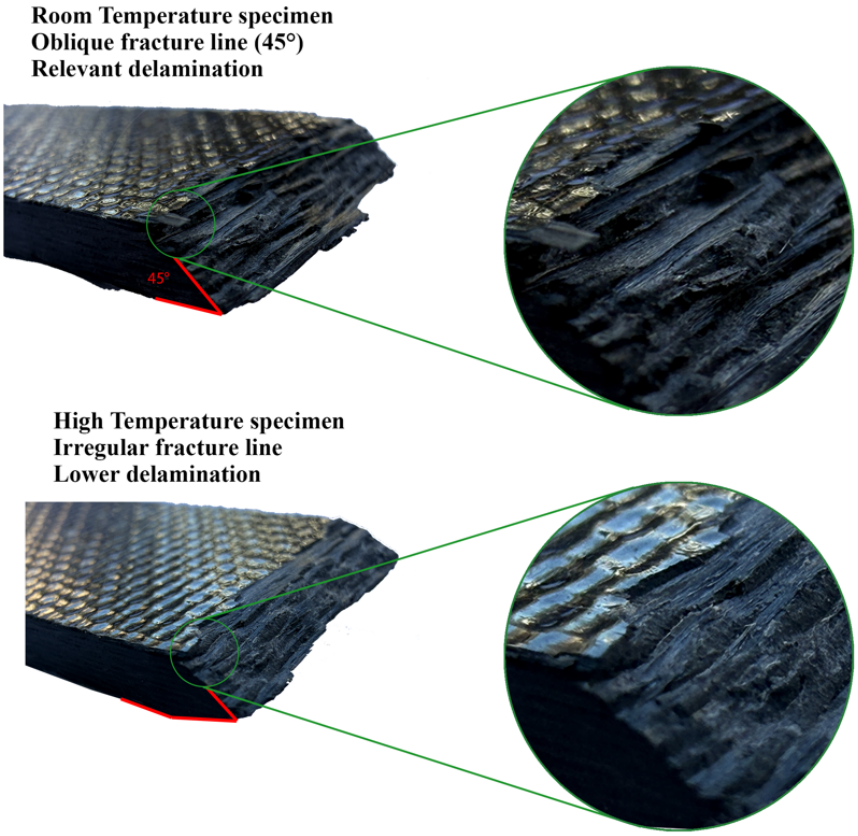

Figure 3.7: Fracture morphology of representative compression specimens (ASTM D695) at room temperature (top) and high temperature (bottom).

3.6. Impact and Compression After Impact (CAI)

Energy Profile Diagram (EPD) :

As previously described in Section 2.3.6, two key parameters are used to characterise the impact response of composite laminates: impact energy E_i and absorbed energy E_a. Their relationship is represented through an Energy Profile Diagram (EPD), which supports the identification of critical transitions such as penetration and perforation.

For each discrete impact energy level, the absorbed energy was determined as the arithmetic mean of the four experimental replicates.

Figure 3.8 reports the EPD for the twill fabric laminate investigated in this work. For reference, the so-called equal energy line ($E_a = E_i$) is represented.

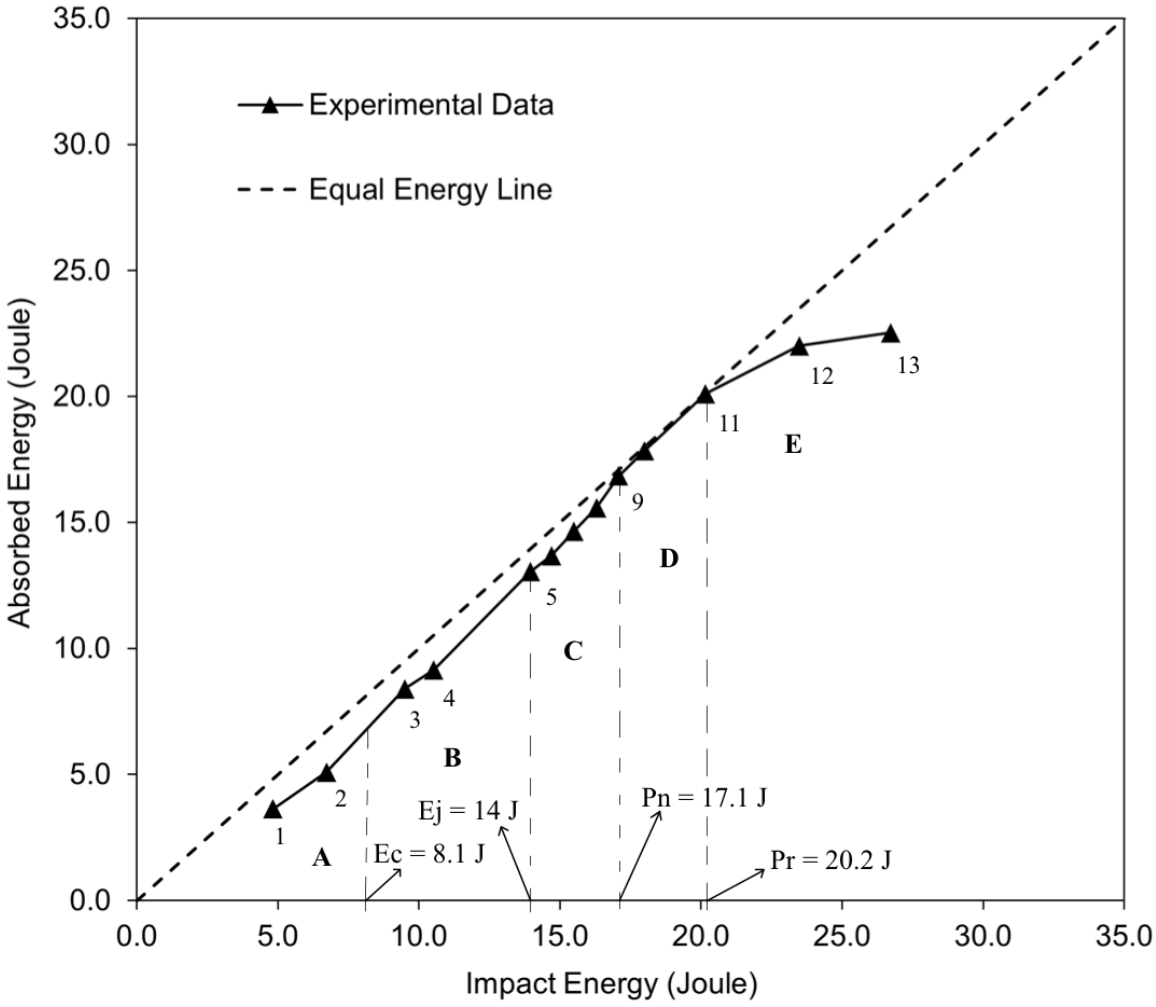

Figure 3.8: Energy Profile diagram (EPD) for the investigated twill fabric composite.

The data points can be divided into five regions (A–E) indicated by dashed lines. Each region corresponds to a distinct stage of damage evolution. By combining post-impact visual inspection, contact force–displacement responses, and EPD, the damage process with increasing impact energy can be detailed as described below.

In Region A, the damage is limited to very small indentation and matrix cracking on the impacted face (Barely Visible Impact Damage (BVID)). In this regime, the difference $E_i - E_a$ is significant because the excess energy is retained in the impactor and used to rebound at the end of the contact event [41, 48].

As the impact energy increases to the intersection point between Region A and Region B, bending-driven fibre breakage begins to appear on the non-impacted face, and the difference $E_i - E_a$ reduces. This intersection point is defined as the critical damage threshold $E_c = 8.1$ J for the transition between Region A and Region B. In Region B, indentation and matrix cracking continue to grow, but bending fracture of fibres is recognised as the dominant damage mode. This region is characterised by increased damage compared to Region A, but still without penetration, with the delamination becoming progressively more evident towards the upper end of the region.

Region C begins at $E_j = 14$ J and is dominated by increased delamination as the impact energy increases. Region C is defined as the region where the trend remains parallel to the equal energy line [41, 48, 49]. This indicates that the difference $E_i - E_a$ is approximately constant and that the additional impact energy introduced in this region is absorbed by the laminate as the impactor enters deeper into the structure [41, 48]. Although matrix cracking continues to develop, delamination governs the response in this region. Penetration becomes possible once the delamination has extended to the full thickness of the laminate [41].

The onset of penetration is identified in data point 9 (Region D). The penetration threshold can be defined as $P_n = 17.1$ J. In the EPD, this corresponds to the first point on the equal energy line, indicating that there is no excess energy left and the entire impact energy is absorbed by the laminate [41, 48, 49]. As penetration progresses, additional energy is required for further advancement of the impactor into the material. The penetration range is proportional to the thickness of the laminate [48]. Perforation occurs when fibre failure reaches a critical extent and can no longer sustain load transfer.

Finally, Region E represents perforation, with data point 11 defining the perforation threshold $P_r = 20.2$ J. The perforation threshold corresponds to the last data point on the equal energy line [41, 48, 49]. Once perforation occurs, any impact energy in excess of this threshold is expended in friction in driving the impactor through the damaged laminate rather than being returned as rebound. Therefore, after perforation, absorbed energy remains practically constant. P_r can be treated as a material constant for the given laminate [48].

Contact Force-Displacement (F–d) Curves :

Contact force–displacement (F–d) curves under various impact energies are the signature of the composite material response to impact loading. The contact force is defined as the compressive load exerted by the specimen on the impactor during the contact dura-

tion. The F–d curves give significant information in relation to the impact behaviour of composite laminates, such as rebounding, penetration, and perforation.

As anticipated in section 2.3.6, F–d curves are classified into two categories: closed-type and open-type. A closed-type curve indicates a rebound event, where the curve returns to the origin, signifying that the impactor has bounced off the specimen. Conversely, an open-type curve is characteristic of perforation: the displacement continues to increase as the impactor passes through the material, preventing a return to the zero displacement state.

Figure 3.9 summarises the F–d responses for the DC batch across the energy range considered. For the sake of clarity, a single representative curve has been selected for each impact energy level.

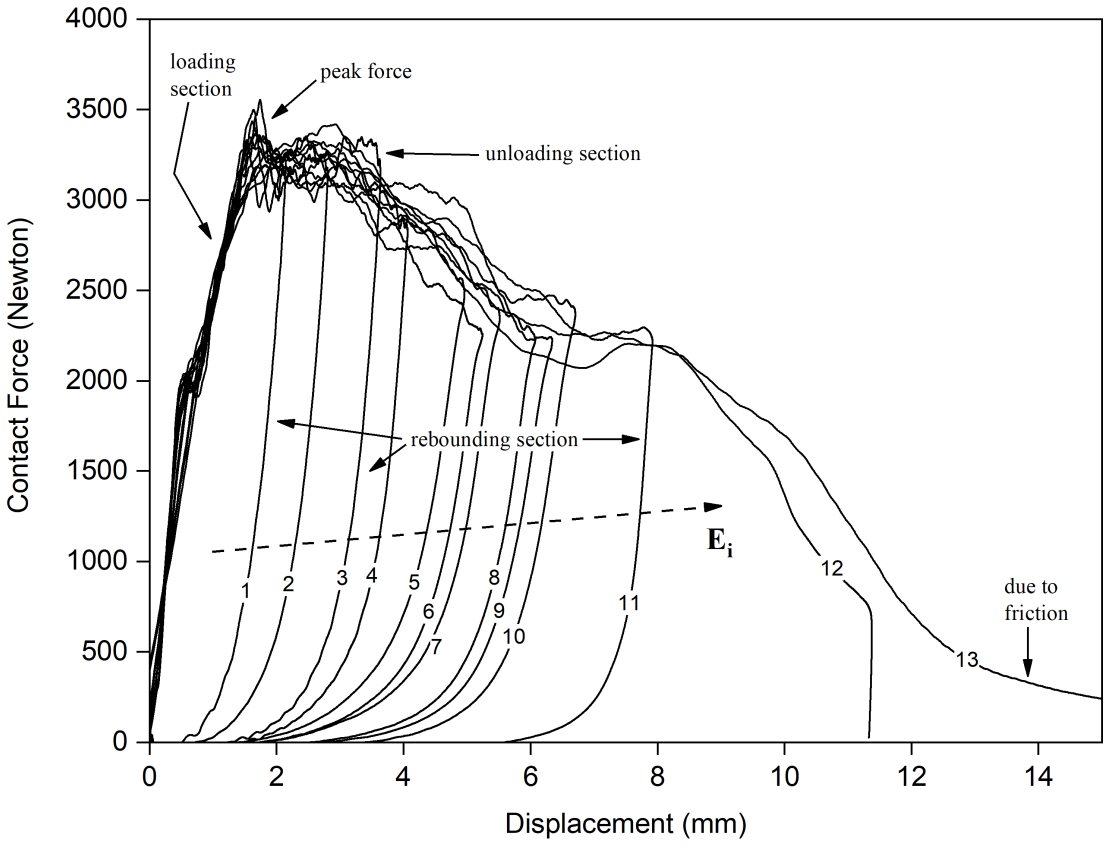

Figure 3.9: Contact force-displacement curves for DC batch.

The curves presented in Figure 3.9 have been artificially smoothed to enhance the visual clarity of the primary trends. However, raw, unsmoothed data were strictly used for the calculation of quantitative parameters (i.e., E_a and P_c), to ensure that no relevant physical information was lost during signal processing (see Section 2.3.6).

The morphology of the F–d curves can be divided into three distinct stages. First, the ascending stage: this initial slope represents the apparent bending stiffness of the laminate. In this phase, the material resists the movement of the impactor through elastic deformation (bending) and initial micro damage.

The second and intermediate stage of the F–d curve is characterised by a force plateau and oscillations in the contact force. In particular, these two features were interpreted as indicators of damage events associated with sudden reductions in bending stiffness. They serve as a primary indicator of the accumulation of internal damage, and highlight the material's capacity for energy dissipation [49]. In fact, the laminate expends the impactor's kinetic energy through the creation of new fracture surfaces (i.e., matrix cracking, bending fracture of fibres and delamination) [49]. The length of the plateau increases as the damage accumulates. Moreover, the oscillations observed along the load path reflect the dynamic and vibratory nature of the impact event. They represent a momentary loss of contact between the impactor and the specimen surface (some high-frequency fluctuations are also related to the inevitable vibrations of the specimen and the test fixture) [41]. This dynamic phenomenon follows a "contact–damage–loss of contact" sequence. It is triggered by a sudden internal failure, such as large delamination or fibre rupture. This failure then causes a rapid localised deformation that eventually exceeds the instantaneous velocity of the impactor. This results in a transient drop in the recorded force followed by a subsequent "re-load" once contact is re-established, creating the pulsated appearance characteristic of impact F–d curves.

Lastly, the descending stage. In rebound events, characterised by closed curves, the descending slope represents the return of the impactor towards the initial zero-displacement position. In perforation events resulting in open curves, the unloading region is characterised by a frictional tail. This residual force originates from the friction between the impactor and the damaged laminate as the impactor passes through the specimen.

As in the EPD, the F-d curves can also be divided into the five characteristic damage stages (A–E), each corresponding to a change in the morphology of the F-d curves (see Figure 3.10).

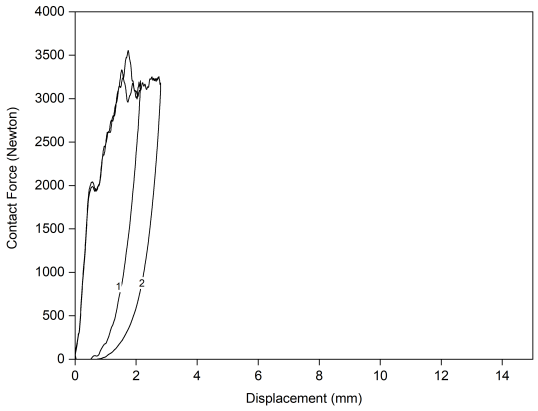

(a) Region A: BVID.

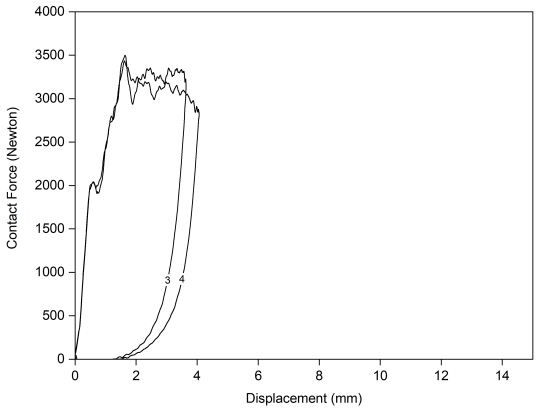

(b) Region B: Bending fracture of fibres (at non-impacted face).

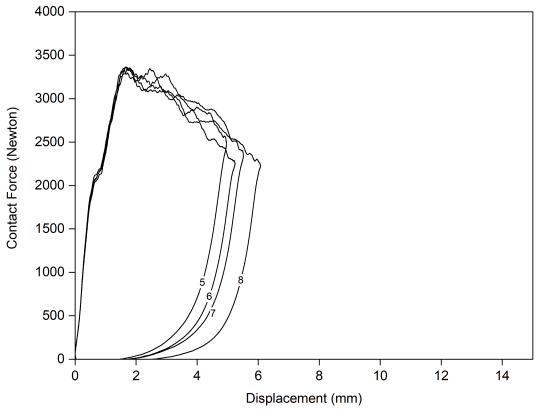

(c) Region C: Delamination growth.

Figure 3.10: Representative contact force–displacement curves for the DC batch across impact energy regions (Part I: Regions A, B, and C).

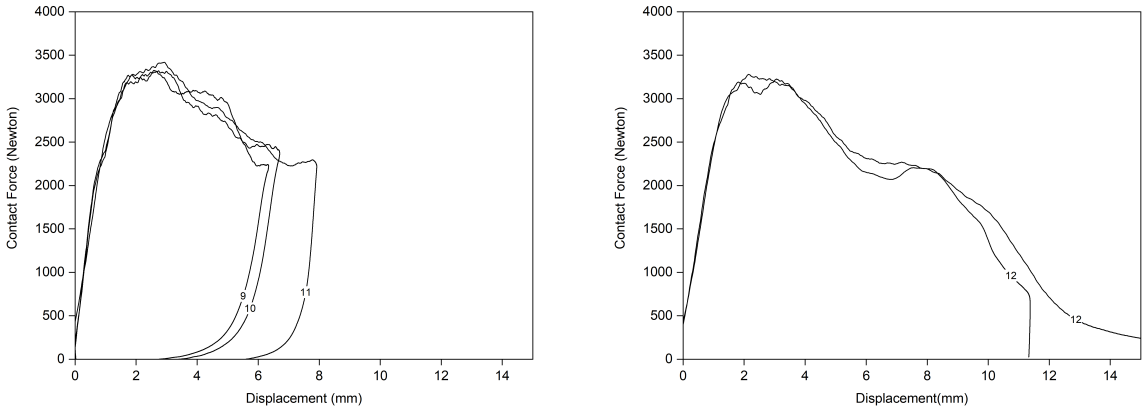

(d) Region D: Penetration.

(e) Region E: Perforation.

Figure 3.10: Representative contact force–displacement curves for the DC batch across impact energy regions (Part II: Regions D and E).

Region A corresponds to Barely Visible Impact Damage, where minor surface indentation and matrix cracking dominate. The F–d curves are closed, and descend as soon as the peak force is reached, indicating rebound and a largely elastic response. In this low damage regime, the maximum contact force $F_{\max}$ increases with increasing impact energy E_i, consistent with the laminate retaining most of its structural integrity.

With an additional increase in E_i, Region B marks the onset of tensile fibre fracture due to bending on the non-impacted face. These mechanisms reduce local bending stiffness and are reflected in the F–d response by developing a force plateau and oscillations near the maximum force. The length of the plateau increases as the damage accumulates. Delamination becomes more significant towards the end of the region. In this regime, $F_{\max}$ becomes independent of further increases in E_i.

Region C is governed by delamination growth: this produces a significant reduction in structural integrity, which appears as a steep drop in contact force after $F_{\max}$. This distinguishes Region C from the more gradual plateau-type behaviour observed in Region B, indicating a transition towards more critical damage.

Once the penetration threshold is reached (Region D), the depth of penetration increases proportionally with impact energy, and the F–d curves become progressively open. The failure of the curve to return to the origin reflects incomplete rebound.

Finally, Region E corresponds to perforation, where the F–d curves are fully open, and the

impactor traverses the laminate. Beyond this threshold, additional energy is dissipated through friction associated with the impactor moving through the specimen.

Critical Treshold Force for the Onset of Delamination (P_c) :

Regarding P_c, the impact failure process in these woven fabric laminates can be divided into two distinct stages. Firstly, the initiation of damage, and secondly, the subsequent propagation of damage throughout the structure. Damage initiation occurs only when the contact force reaches a specific threshold (P_c). If the incident energy is insufficient to overcome this force, no detectable or visible damage is produced, and the response remains essentially elastic.

The relationship between P_c and the incident impact energy is illustrated in Figure 3.11. For each discrete impact energy level (E_i), the threshold force (P_c) was determined as the arithmetic mean of the four experimental replicates.

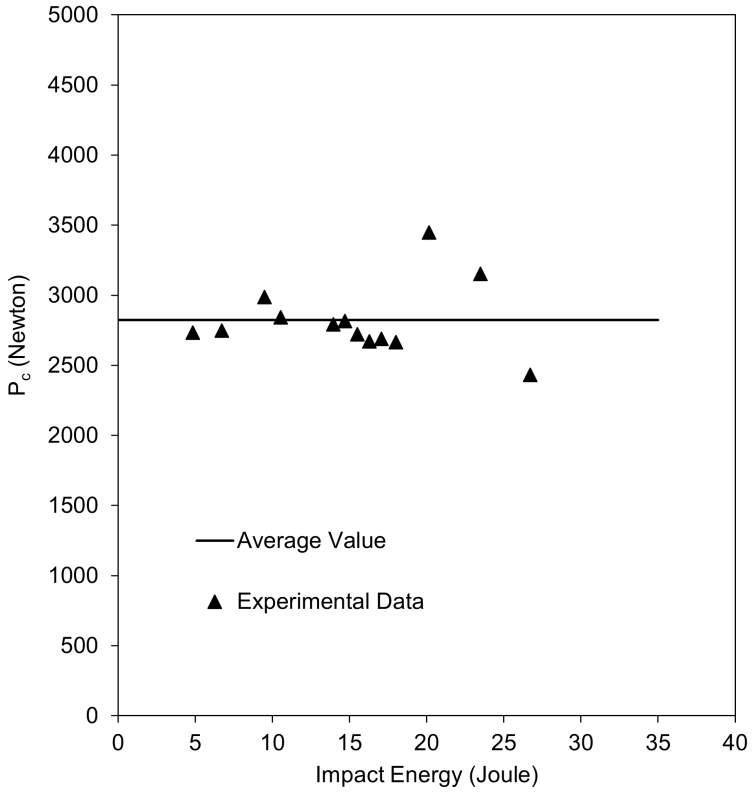

Figure 3.11: P_c for varied impact energies for the DC batch.

For the laminates studied, the experimental data indicate that P_c is independent of the

impact energy throughout the majority of the testing range. This observation is consistent with established literature [42]. This suggests that the threshold force is a characteristic of the material, rather than a function of the specific impact event. Similarly, the magnitude of the initial load drop and the frequency of subsequent load oscillations were found to be intrinsic characteristics of the composite material and independent of impact energy [42].

A deviation from the average value is observed at the three highest impact energy levels. This variation in P_c is likely an artifact of distorted F–d profiles associated with the onset of perforation. In these high-energy regimes, rapid penetration of the impactor makes the identification of the first critical load drop less distinct, appearing to shift the threshold force to anomalous values.

Displacement vs. Time (d–t) curves :

Figure 3.12 presents the displacement–time (d–t) curves for the investigated specimens. For the sake of clarity, a single representative curve has been selected for each impact energy level.

For non-perforated specimens, the rebound event is captured in the d–t curves as a return to the baseline (initial contact position). Furthermore, the time required for the impactor to return to its initial contact position increases as E_i increases. This extended return duration is a direct consequence of increasing damage: as more energy is expended in creating new fracture surfaces, the rebound velocity is attenuated.

In contrast, perforated specimens are characterised by a continuous increase in displacement that never returns to the baseline, indicating that the impactor has completely traversed the material.

A comparison between the experimental F–t and the d–t curves reveals a distinct temporal shift: the maximum displacement ($d_{\max}$) is reached later than the maximum contact force ($F_{\max}$). Physically, $d_{\max}$ corresponds to the point at which the impactor's velocity reaches zero, representing the full conversion of kinetic energy. In contrast, $F_{\max}$ identifies the moment of maximum structural resistance that precedes the onset of significant material failure.

This time delay is listed in Table 3.16 for non-perforated specimens, as perforated samples exhibit a continuous increase in displacement that does not return to zero. The delay between $F_{\max}$ and $d_{\max}$ is attributed to the impactor's inertia, which causes it to continue to move downward even after the laminate has reached its maximum load-carrying capacity [41]. This temporal shift becomes more pronounced with increasing impact energy, reflecting progressive damage.

As shown in the data, the time to reach the peak force (t at $F_{\max}$) remains constant, oscillating around 0.9 ms independently of the impact energy. Once again, this behaviour suggests that the damage threshold is an intrinsic characteristic of the material system.

Table 3.16: Time to reach $d_{\max}$ and $F_{\max}$ for increasing impact energy.

E_i [J]	t at $d_{\max}$ [ms]	t at $F_{\max}$ [ms]	Δt [ms]
4.8	2.115	1.206	0.909
6.7	2.757	0.912	1.845
9.5	3.636	0.918	2.718
10.5	4.140	0.915	3.225
14.0	6.080	0.925	5.155
14.7	5.950	1.205	4.745
15.5	6.340	0.910	5.430
16.3	6.330	0.900	5.430
17.1	8.240	0.944	7.296
18.0	8.104	1.032	7.072
20.2	6.424	0.704	5.720

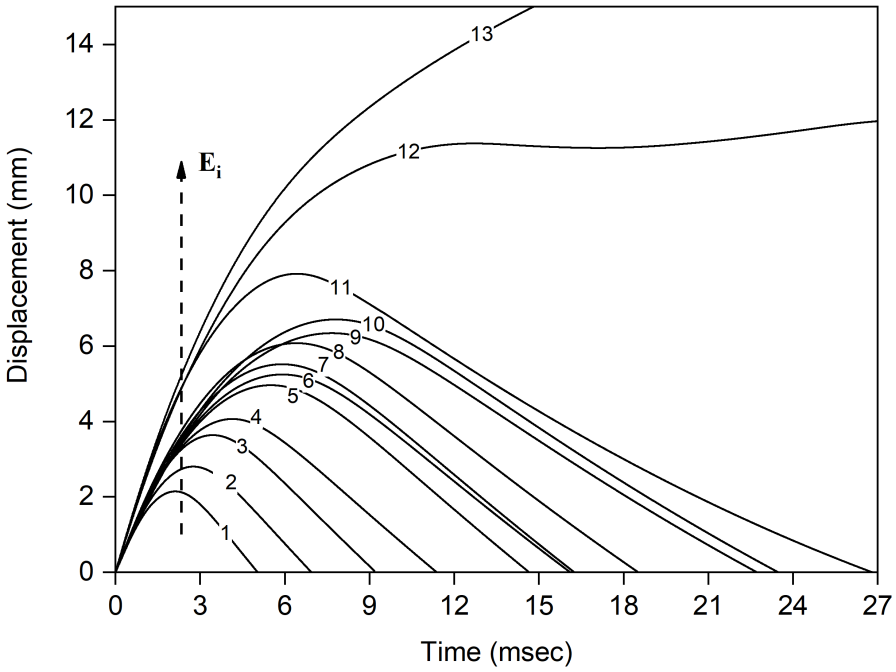

Figure 3.12: Variation of displacement vs. time at varying impact energies for the DC batch.

Absorbed Energy vs. Time (E_a-t) Curves :

The temporal evolution of the energy transferred to the composite specimens is presented in Figure 3.13. For the sake of clarity, a single representative curve has been selected for each impact energy level.

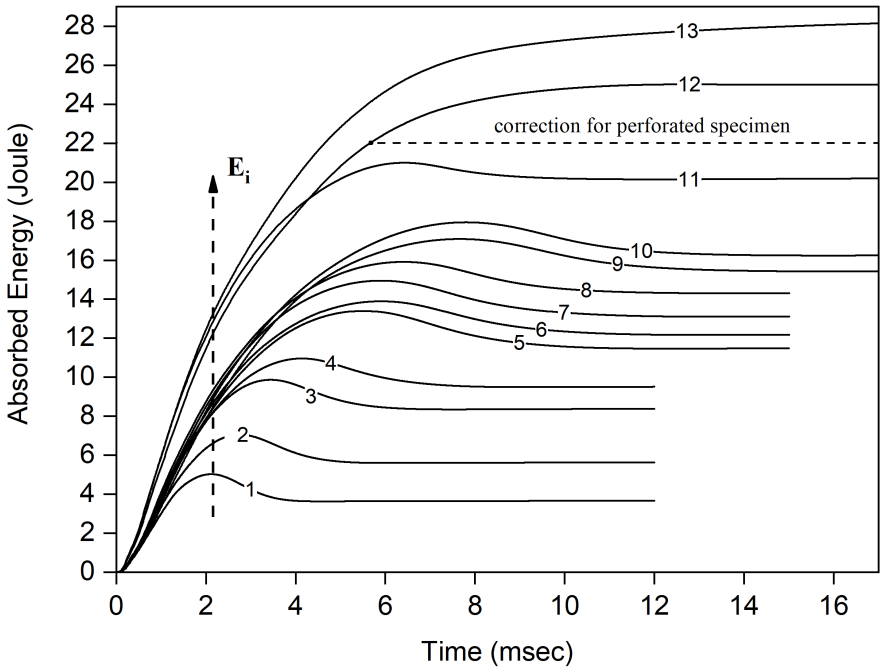

Figure 3.13: Variation of absorbed energy vs. time at varying impact energies for the DC batch.

The total energy absorbed by the specimen increases proportionally with the impact energy (E_i). This trend is attributed to the increased severity of internal damage, which dissipates a larger fraction of the kinetic energy of the impactor.

Each curve initially increases during the loading phase until it reaches a maximum value (E_{max}). In non-perforated cases, the curve then decreases during the unloading phase before stabilising at a constant horizontal plateau. This final plateau represents the total absorbed energy (E_a). The difference between the peak value (E_{max}) and the final plateau (E_a) represents the excessive energy; this difference of energy is retained and used to rebound the impactor from the non-perforated specimens.

For specimens where perforation occurs, the energy recorded after the initial failure includes the work done by friction as the impactor traverses the laminate. To isolate the energy associated strictly with material damage, post-perforation friction was neglected. Consequently, the E_a–t history was corrected as indicated by the dashed line in Figure 3.13 (exemplified for specimen 12), representing the actual energy dissipated during the

impact event.

Velocity vs. Time Trend :

The kinematic behaviour of the impactor, specifically the velocity–time relationship, provides another interpretation of the damage process.

At the onset of impact ($t = 0$), the velocity is at its maximum value, corresponding to the initial impact velocity v_i. As the contact event progresses, the velocity decreases as the kinetic energy is dissipated through material damage.

For non-perforated specimens, the velocity continues to decrease until it reaches zero, at the moment of maximum displacement ($d_{\max}$). Following this point, the velocity becomes negative, indicating the start of the rebound phase. The absolute value of this negative velocity increases with time, eventually stabilising at a constant rebound velocity (v_r).

In contrast, the velocity–time profiles of the perforated specimens never cross into the negative regime. In these cases, the velocity decreases as the impactor traverses the laminate but remains positive throughout the entire event. The absence of a negative velocity component implies that there is no rebound.

Another parameter in describing impact is the ratio of rebound velocity to initial impact velocity ($|v_r|/v_i$). This ratio serves as a direct measure of the elasticity of the contact event and the extent of energy dissipation within the laminate. The ratio $|v_r|/v_i$ decreases as the impact energy increases [41]. This decline is a physical manifestation of the increasing damage within the specimen. In fact, as more energy is consumed by fibre breakage, matrix cracking, and delamination, less energy remains available to be returned to the impactor. This trend is clearly visible in Table 3.17, which shows the ratio $|v_r|/v_i$ for each impact energy. For each discrete impact energy level (E_i), the ratio $|v_r|/v_i$ was determined as the arithmetic mean of the four experimental replicates.

In a theoretical purely elastic impact, where no energy is dissipated through damage, the ratio $|v_r|/v_i$ would equal 1 [41]. For very low impact energies (below those corresponding to $E_i = 4.8$ J), the ratio remains near unity, reflecting a nearly perfect elastic recovery. However, as the impact energy progresses into the penetration and perforation regimes, the ratio drops towards zero. In the case of perforation, the impactor does not rebound at all, which means that there is no negative velocity component; therefore, $|v_r|/v_i$ is effectively zero [41].

Table 3.17: $|v_r|/v_i$ ratios for the DC batch at different energy levels.

Specimen	E_i [J]	$\|v_r\|/v_i$ Ratio
1	4.8	0.52
2	6.7	0.45
3	9.5	0.37
4	10.5	0.36
5	14.0	0.28
6	14.7	0.29
7	15.5	0.27
8	16.3	0.26
9	17.1	0.24
10	18.0	0.23
11	20.2	0.19
12	23.5	0
13	26.7	0

Compression After Impact (CAI) :

Table 3.18 summarises CAI results at room temperature for both batches, reporting the mean residual compressive strength F_{CAI} as a function of impact energy.

Table 3.18: Room temperature Compression After Impact (CAI) results.

Impact Energy	BC Batch		DC Batch	
E_i [J]	Specimens [#]	F_{CAI} [MPa]	Specimens [#]	F_{CAI} [MPa]
0	*N/A*	-	3	245.1 ±2.8
4.8	*N/A*	-	2	164.1 ±2
6.7	*N/A*	-	2	146.6 ±1.1
9.5	10	141.9 ±7.4	2	142.8 ±8.3
10.5	*N/A*	-	2	133.1 ±0.7
14	*N/A*	-	2	131.5 ±0.3
14.7	*N/A*	-	2	120.2 ±1.0
15.5	*N/A*	-	2	123.8 ±3
16.3	*N/A*	-	2	122.5 ±3.7
17.1	*N/A*	-	2	126.6 ±2.2
18	10	137.5 ±6.1	2	119.8 ±1.8
20.2	*N/A*	-	2	123.1 ±0.7
23.5	*N/A*	-	2	111.1 ±3.1
26.7	*N/A*	-	2	117.2 ±3

A preliminary observation concerns the compressive strength of the undamaged sample ($E_i = 0$ J): the compression strength values obtained with ASTM D7137 (CAI) are significantly lower than those obtained with ASTM D695 (245 MPa with ASTM D7137 vs. 335 MPa with ASTM D695).

Considering the damaged conditions, the DC batch exhibits a reduction in compressive strength with increasing impact energy. A significant drop of 33% is observed at the lowest impact level (4.8 J), where the strength falls from 245.1 MPa to 164.1 MPa. As E_i progresses towards penetration and perforation, F_{CAI} approaches a lower limit in the range of 111–120 MPa.

Figure 3.15 shows the relationship between impact energy and residual compressive strength F_{CAI}.

Direct comparison between BC and DC batches is possible at two specific energy levels. At 9.5 J the batches show high convergence, with the BC mean (141.9 MPa) and the DC

mean (142.8 MPa) differing less than 1%. At 18 J a divergence in performance emerges, with the BC batch retaining a higher mean strength (137.5 MPa) compared to the DC batch (119.8 MPa), representing a 13% discrepancy.

The BC batch results are derived from a larger population ($n = 10$), providing a more robust statistical mean. In contrast, the DC batch provides a broader mapping of the degradation curve across 13 energy levels, with a smaller sample size ($n = 2$) per increment.

CAI testing resulted in LDM failure in all impacted specimens: the fracture occurred laterally, through the damage, and at the center of the specimen (see Figure 3.14). This is a commonly observed acceptable compressive residual strength failure mode according to ASTM D7137 [40].

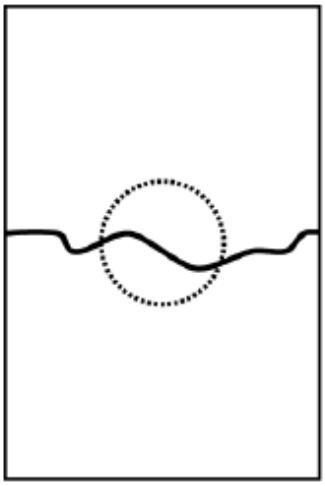

Figure 3.14: LDM (Lateral, through Damage, in Middle) failure mode in CAI tests. The damaged area is shown by the dashed circle.

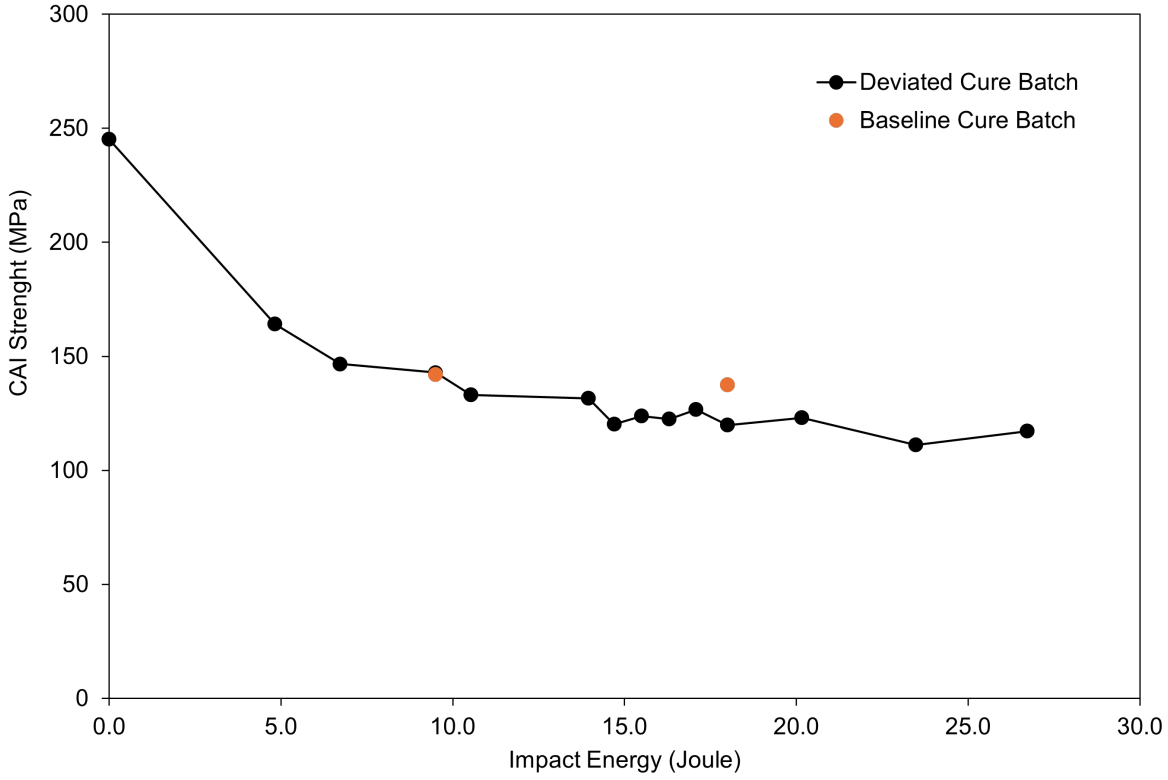

Figure 3.15: Variation of Compression After Impact Strength (F_{CAI}) with impact energy at room temperature.

Table 3.19 summarises the CAI results at high temperature ($T = 120\,°\text{C}$) for the DC batch, reporting the mean residual compressive strength F_{CAI} as a function of impact energy. The same trend is illustrated in Figure 3.16.

Table 3.19: High-temperature ($T = 120\,°C$) Compression After Impact (CAI) results.

Impact Energy	**DC Batch**	
E_i **[J]**	**Specimens [#]**	F_{CAI} **[MPa]**
0.0	3	193.5 ±7.8
4.8	2	139.2 ±4.1
6.7	2	125.6 ±3.8
9.5	2	118.2 ±7.5
10.5	2	121.5 ±5.7
14.0	2	116.5 ±8.1
14.7	2	104.0 ±9.6
15.5	2	107.7 ±1.3
16.3	2	104.8 ±1.9
17.1	2	100.7 ±10.9
18.0	2	99.6 ±0.2
20.2	2	98.9 ±6.4
23.5	2	96.7 ±8.0
26.7	2	102.9 ±7.2

Compared to room-temperature results, F_{CAI} is systematically lower across all impact energies (typically by $\sim$ 10–20%). This indicates a clear temperature sensitivity of the post-impact compressive response.

Another preliminary observation concerns the compressive strength of the undamaged sample ($E_i = 0$J). The results obtained with ASTM D7137 are significantly lower than those obtained with ASTM D695, even when testing at high temperature.

The energy dependence remains qualitatively similar to that at room temperature (Figure 3.16). The undamaged reference condition ($E_i = 0$ J) provides the upper bound ($F_{CAI} = 193.5$ MPa). Increasing the impact energy produces a progressive reduction in residual strength as the severity of the damage increases.

The greatest reduction occurs at low to moderate impact energies (from 0 to about 9.5 J), where F_{CAI} decreases from 193.5 MPa to roughly 118 MPa, indicating a rapid shift towards damage-dominated behaviour. For higher energies ($E_i > 14$ J), the residual

strength tends to level off at approximately 97–108 MPa.

Small non-monotonic variations should be interpreted cautiously because each condition is based on only two repetitions ($n = 2$). At 120°C, additional sources of variability, such as temperature uniformity and increased sensitivity to alignment and fixture as the matrix softens, can further contribute to the scatter.

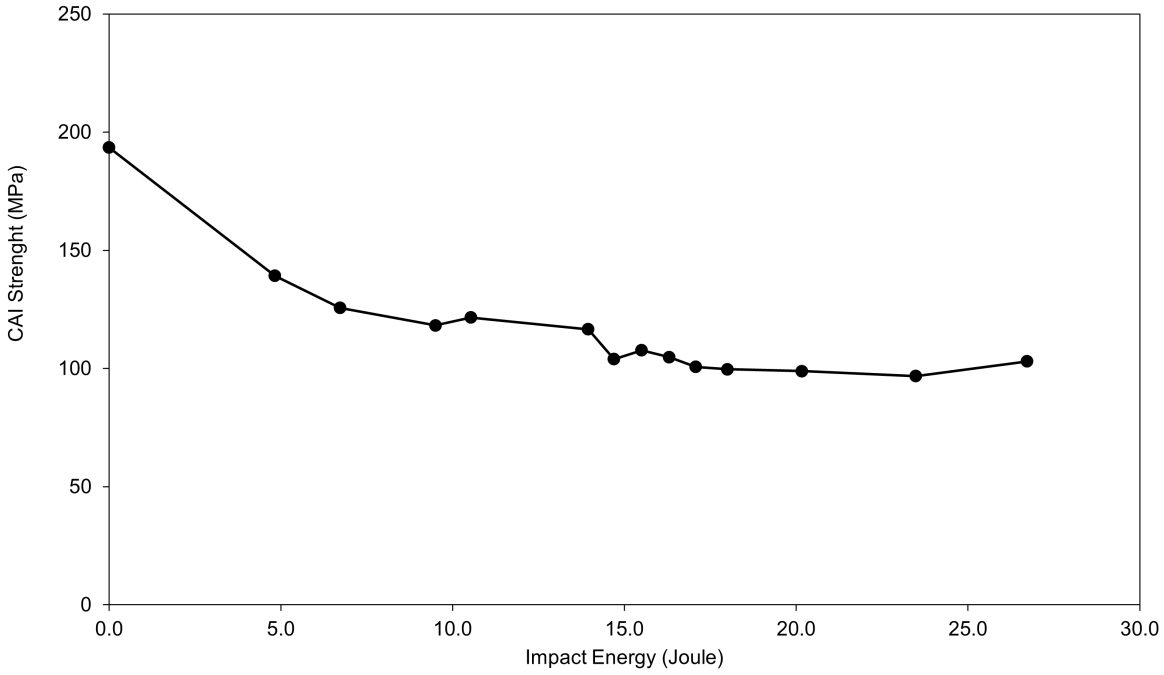

Figure 3.16: Variation of Compression After Impact Strength (F_{CAI}) with impact energy at $T = 120\,°\text{C}$ for the DC batch.

4 | Discussion

The experimental results presented in Chapter 3 provide a comprehensive overview of the thermochemical and mechanical responses of the two batches investigated in this work. This chapter moves beyond a descriptive presentation of the data and develops an interpretation of the trends. By correlating the outcomes of the different test methods, the discussion attempts to explain how the cure-dependent matrix influences the observed behaviour in each test.

Cure State and Thermal Indicators :

The DSC provides the primary evidence that the deviated thermal history reduced the achieved cure state. As shown in Tables 3.1–3.3, the DC laminates retain a larger fraction of unreacted epoxy groups than the BC reference. The residual enthalpy in DC is approximately 5–6 times higher than in BC (51.08 vs. 9.10 J/g), corresponding to a 12% reduction in degree of cure ($DoC \approx 0.86$ for DC vs. $DoC \approx 0.98$ for BC).

The T_g measurements are consistent with this DSC based ranking. The BC batch exhibits a high $T_g \approx 180$°C (Table 3.6), consistent with a nearly complete cure and a highly crosslinked network. On the other hand, the DC batch shows a lower $T_g \approx 140$°C (Table 3.5), consistent with a less densely crosslinked structure associated with the lower DoC calculated with DSC.

Importantly, the magnitude of the T_g reduction (about 40 °C for only a 12% reduction in degree of cure) is not surprising because the T_g–DoC relationship is strongly non-linear [50–53]. As cure approaches completion, small differences in conversion can produce a steep increase in T_g, as captured by DiBenedetto-type formulations [50–53]:

$$T_g = T_{g0} + \frac{(T_{g\infty} - T_{g0})\lambda DoC}{1 - (1 - \lambda)DoC}, \tag{4.1}$$

where T_g is the glass transition temperature at a given degree of cure, T_{g0} is the glass transition temperature of the uncured monomer, $T_{g\infty}$ is the glass transition temperature of the fully cured network, DoC is the degree of cure ($0<DoC<1$), and λ is a structure

dependent parameter ($0 < \lambda < 1$) that describes the progressive restriction of molecular mobility as crosslinks form (i.e., ratio of mobility between the monomer and the fully cured polymer). A typical trend predicted by the DiBenedetto equation is shown in Figure 4.1.

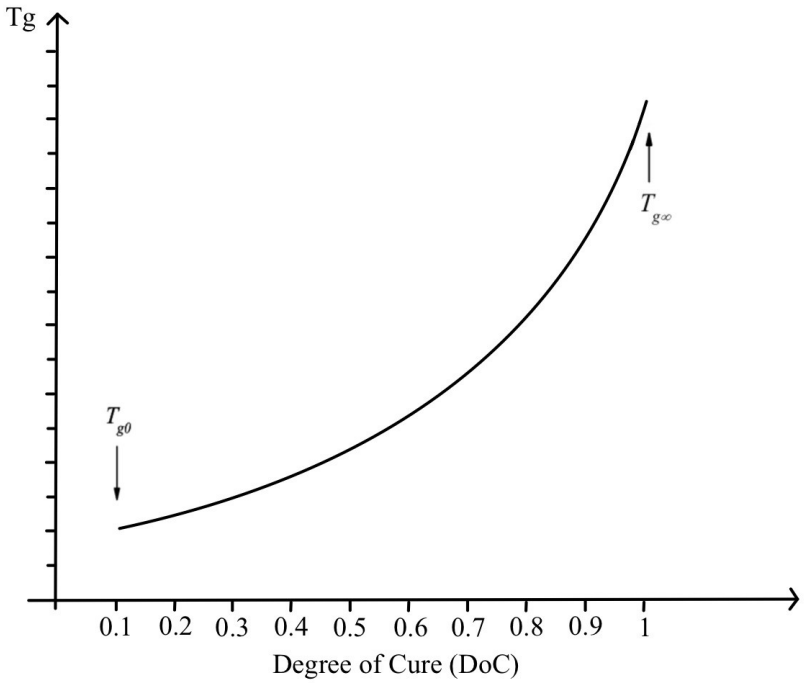

Figure 4.1: Typical trend of DiBenedetto equation.

The TMA results provide complementary indications of the matrix state, particularly in the through-thickness direction, where thermal expansion is matrix-dominated. The relatively high α_r recorded by TMA is consistent with the undercured condition of the DC batch ($DoC \approx 0.86$). In fact, a lower DoC implies a reduced crosslink density [50–53], and therefore greater chain mobility and greater thermal expansion once the glass transition temperature is exceeded. In conclusion, the lower DoC increases the material's change in free volume with temperature.

This interpretation is reinforced by the large dispersion observed in the rubbery region in the through-thickness direction (e.g., specimen 3 at 145.6 vs. specimen 4 at 204.4×10^{-6} $^{\circ}C^{-1}$). This dispersion suggests that the faulty cure cycle caused chemical heterogeneity within the resulting laminate; consequently, different regions of the laminate may have reached different local $DoCs$, producing a non-homogeneous expansion response.

Together, the trends of DSC, T_g, and TMA indicate that the BC cycle produced a fully developed and uniform network. On the other hand, the DC cycle, despite the subsequent cure attempt, did not fully restore conversion and yielded a lower and more variable

thermal response. This last behaviour is consistent with incomplete network formation after an interrupted cure history [8–10].

The thermochemical results support the interpretation that the interruption in the DC cycle occurred late in the reaction, near or after gelation/vitrification. As a result, the cure resumption (4 days later) could not reproduce the same resin flow and consolidation conditions available earlier in the cycle.

Considering the resin content, the numerical results in Tables 3.7 and 3.8 show that the difference between the means of the batches is small (0.5 wt%), indicating that the two curing routes produced laminates with a comparable resin content. Both batch means fall within the nominal prepreg range (40 ± 3 wt%) [21]. Minor specimen-to-specimen differences can still occur even with unchanged vacuum bagging, because of (i) small variations in local compaction and resin flow prior to gelation (e.g., local bag bridging/wrinkling or small differences in vacuum quality); (ii) thermal history effects on resin viscosity and mobility; (iii) sampling variability across the panel.

Consistently, Test Method II applied to the panel reference yields a resin content close to the nominal value (Table 3.9). Finally, the small discrepancy observed between Test Method I and Test Method II in Tables 3.7–3.9 is expected. In fact, thickness-based calculations assume negligible void content, and depend on (i) thickness and density measurement uncertainties and (ii) areal-weight tolerances. In contrast, Test Method I is based on the recovered fibre mass after matrix removal.

Compression Behaviour :

The room-temperature compression results show that the most distinctive feature of the DC batch is the larger scatter visible in Tables 3.12 and 3.13.

This dispersion is once again consistent with the faulty thermal history, which likely introduced chemical heterogeneity and yielded a less uniform laminate. As a consequence, the resin locally provides less consistent lateral support to the fibres and less effective load transfer. This increases sensitivity to local laminate features and promotes greater variability in matrix failure and interface-controlled failure. At the same time, part of the scatter can be methodological: the ASTM D695 end-loaded configuration is known to be more sensitive to alignment, seating, and end effects than the ASTM D6641 CLC fixture [34, 54, 55].

Despite the reduced cure state of DC, the room-temperature compression data do not show a clear decrease in the mean modulus, and the mean strengths remain of comparable magnitude. The stability of the mean modulus is consistent with the general expectation that

the stiffness measured well below T_g is relatively insensitive to the cure state [11]. In contrast, compressive strength (F_{cu}) is more dependent on matrix and interlaminar integrity, as well as on the specific test fixture; therefore, its interpretation requires additional care, especially since the two batches were tested using different standards (ASTM D6641 for BC vs. ASTM D695 for DC).

As anticipated, compression properties in polymer composites are strongly method dependent. Premature failure can be triggered by non-intrinsic effects that are not solely governed by the material state; for example, stress concentrations, parasitic bending, and buckling [34, 54, 55]. Consistently, comparative studies report mixed trends. In some cases, the D695-end-loading yields strengths comparable to or higher than those of other methods. In contrast, other surveys report higher values for CLC/D6641 [34, 56–60]. For this reason, the lack of a marked reduction in the mean DC compressive strength does not, by itself, rule out a mechanically relevant undercure. If the specific implementation of ASTM D695 in this campaign tends to overestimate the strength relative to D6641, apparent strength retention could be partially methodological. Under this interpretation, the increased scatter in DC, together with the reduced cure state indicated by thermochemical evidence, provides a more robust indication of compromised matrix/interlaminar integrity rather than mean strength values alone.

Macroscopic fracture observations and the trends in Tables 3.10–3.13 suggest a room temperature progression of failure consistent with established compressive damage mechanisms. Fibres are initially loaded in axial compression; with increasing load, local fibre microbuckling initiates in regions of misalignment and/or local weakness of the matrix; microbuckling promotes matrix cracking, which then facilitates interlaminar crack growth and delamination, consistent with the extensive delamination observed macroscopically [46].

At elevated temperature, the reductions reported in Tables 3.14 and 3.15 are consistent with the temperature-driven degradation of the interface and matrix performances [44]. The mismatch between the thermal expansion of the constituents can introduce internal stresses, while resin softening promotes matrix cracking and reduces the efficiency of load transfer [45]. The appearance of the fracture surface at high temperature supports this interpretation: matrix softening reduces lateral confinement, favouring a failure process controlled by buckling/kinking; delamination is still present, but appears less pronounced than in room temperature specimens. Therefore, fibre instability and local kinking dominate the final failure mode as the matrix approaches the glass transition region [46, 47].

Impact and Compression After Impact Behaviour :

The evolution of impact damage and the associated thresholds have been discussed in Section 3.6; here it is important to recall that the shape of the Energy Profile Diagram depends on both impactor and target characteristics. This includes constituent materials, fibre architecture and geometrical arrangement, laminate thickness, and impactor geometry [41].

Recalling the CAI results, a preliminary observation refers to the undamaged condition ($E_i = 0$ J): the compressive strengths obtained using ASTM D7137 are substantially lower than those obtained from ASTM D695, both at room temperature and $T = 120°$C. This discrepancy is attributed to the ASTM D7137 fixture–specimen configuration and the associated unacceptable failure mode for $E_i = 0$ J. All undamaged specimens tested in the CAI fixture failed by end crushing at the bottom interface (i.e., premature failure in the load-introduction region where local through-thickness stresses exceed the transverse strength before the gauge section reaches its intrinsic compressive limit). This behaviour is promoted by stress concentrations at the specimen–fixture contact, small edge gaps, non-uniform lateral support at the specimen ends, and minor misalignment. Therefore, the results of ASTM D7137 at $E_i = 0$ J should be interpreted as a conservative lower bound governed by the fixture/specimen interface rather than as the true compressive strength of the laminate.

At room temperature, for impacted specimens, the DC batch shows the expected reduction in residual strength with increasing impact energy. A pronounced drop is observed at the lowest impact level (from 245.1 MPa at 0 J to 164.1 MPa at 4.8 J; i.e., -33%); advancing towards penetration and perforation, the values of F_{CAI} approach a lower bound in the range of approximately 111–120 MPa. This response is characteristic of CFRP laminates, where the initial increase in impact energy creates critical damage that severely compromises the residual stability. However, further increases in energy mainly increase the damaged area without producing a proportional decrease in the residual compressive strength [17, 61]. Once the damage has effectively "saturated" the specimen, more energy is expended in friction and penetration processes rather than further reducing residual compressive stability [17].

Comparing BC and DC at the shared room temperature impact energies suggests two regimes. Despite the lower cure state of DC, at moderate impact energy (9.5 J), the residual strengths are essentially identical (142.8 MPa for DC vs. 141.9 MPa for BC). This is consistent with both laminates operating well below their respective T_g values, so that the matrix remains sufficiently stiff to support load transfer and constrain local in-

stability. At higher impact energy (18 J), a clearer separation emerges, with BC retaining higher residual strength (137.5 MPa) vs. DC (119.8 MPa), corresponding to a reduction of 13%. One interpretation is that the lower degree of cure in DC ($\approx$ 0.86) vs. BC ($\approx$ 0.98) increases susceptibility to matrix and interface-controlled damage under more severe impacts (e.g., greater delamination growth and more extensive cracking). Since CAI is strongly governed by delamination-driven instability, small differences in damage morphology can translate into measurable differences in F_{CAI}. However, this comparison should be treated with caution because the 18 J impact configurations were not strictly matched: BC achieved 18 J using a higher velocity (2.56 m/s), while DC used a lower velocity (1.8 m/s) with increased mass. At fixed nominal energy, higher-mass/lower-velocity impacts generally increase contact duration (i.e., extensive energy propagation), promoting a more bending-dominated response that can favour wider delamination growth and a larger damage footprint. In contrast, a lower-mass/higher-velocity impact tends to be more indentation-dominated, with more localised damage and, in extreme cases, a greater tendency towards perforation. This interpretation is consistent with the post-impact observations in this campaign (perforation and localised damage for the higher-velocity condition, vs. non-perforating response with larger delamination/damaged area for the lower-velocity/higher-mass condition).

Finally, the high-temperature CAI results for DC confirm the relevant temperature sensitivity: F_{CAI} is systematically lower at 120 °C ($\sim$ 10–20% throughout the investigated energies). As the temperature approaches the measured T_g of DC, the softening of the matrix reduces the interlaminar load transfer and the ability to restrain the instability driven by delamination. At high temperature, the same overall energy dependence is preserved. In fact, the greatest reduction occurs from 0 to about 9.5 J (193.5 MPa to $\sim$ 118 MPa), indicating a rapid transition towards damage dominated by delamination; while for higher energies ($E_i > 14$ J) the residual strength levels off at approximately 97–108 MPa. Similarly to the room temperature case, once damage has effectively "saturated" the specimen, more energy is expended in friction and penetration processes rather than producing a proportional additional reduction in F_{CAI} [17, 61].

5 | Conclusions and Future Work

This thesis investigated how an interruption of the autoclave during curing, resulting in a faulty cure, affects the thermochemical state and mechanical performance of an aerospace-grade woven CFRP prepreg laminate (Toray TC250 epoxy reinforced with M46J 2×2 twill).

Two laminate batches were considered:

- Baseline Cure (BC): manufactured according to the recommended cure cycle (heating rate of 1 °C/min, dwell at 88±5 °C for 60 min, followed by a hold at 130±3 °C for 2 h, followed by post-cure at 177±5 °C for 2h)
- Deviated Cure (DC): affected by an unplanned interruption during the first hold at 130 °C, followed by the application of the recommended cure cycle several days later.

The operating context requires mechanical and thermal integrity in a range of −50 °C to +150 °C.

The experimental campaign combined thermochemical and thermomechanical indicators: DSC to quantify residual enthalpy and degree of cure; TMA to measure CTE and T_g for DC; DMA to measure T_g for BC; determination of the constituent content; compression testing; low-velocity impact and Compression After Impact testing. All tests were performed following the relevant ASTM standard practices for each method.

DSC provides the clearest evidence that the deviated thermal history reduced cure completion: DC retained a much larger residual enthalpy than BC, with $H_r = 51.08$ J/g for DC vs. 9.10 J/g for BC, corresponding to $DoC \approx 86\%$ (DC) vs. $DoC \approx 98\%$ (BC). The glass transition results are consistent with this ranking: DC exhibits $T_g \approx 140$ °C with higher scatter, while BC exhibits $T_g \approx 180$ °C with limited scatter. These absolute values also align with the trend of the TC250 datasheet, where $T_g \approx 140$ °C is associated with the standard cure at 130 °C, while $T_g \approx 180$ °C is associated with an elevated temperature post-cure at 177 °C. This means that the cure resumption (4 days after the interruption) did not restore the intended laminate DoC and T_g.

The BC batch meets the thermal requirement reported in the material TPS (i.e., $T_g \geq 175\,°C$; see Table 2.2), while the DC batch does not. With $T_g \approx 140\,°C$, DC falls below the minimum threshold and therefore does not meet the required thermal margin for aerospace applications (operating temperatures up to 150 °C).

The CTE results reinforce the picture of a less uniform and undercured matrix state in DC. In the through-thickness direction (matrix-dominated response), the post-transition CTE reaches values up to $204.4 \times 10^{-6}\ °C^{-1}$, with substantial scatter across specimens. The high α_r is consistent with the undercure: a lower DoC implies a reduced crosslink density, and therefore greater chain mobility and greater thermal expansion after T_g. In conclusion, this lower DoC increases the material's change in free volume with temperature.

Together, the higher dispersion in T_g and α_r supports the presence of chemical heterogeneity due to the defective cure cycle in DC: different regions of the same laminate may have reached different local network states, producing a non-homogeneous response.

Measurements of the constituent content indicate that the two cure routes produced laminates with comparable resin content: the batch means differ by only 0.5 wt%, and both lie within the nominal prepreg range (see Table 2.2). This reduces the likelihood that the observed thermal differences arise from a gross change in fibre/resin fraction.

Despite the clear reduction in cure state for DC, the compression dataset does not show a clear decrease in the mean modulus, and the mean strengths remain of comparable magnitude. This is consistent with the expectation that stiffness and strength measured well below T_g are relatively insensitive to the cure state. The most diagnostic feature of the DC compression results is instead the increased scatter, which is again consistent with a less uniform matrix/interlaminar network. It is important to note that BC and DC were tested using different standards (D6641 vs D695), which limit strict comparison of absolute values. In fact, part of this scatter may also be methodological because ASTM D695 end-loading is more sensitive to alignment/seating/end effects than combined loading fixtures.

At elevated temperature (120 °C), DC shows the expected reduction in compressive strength and a failure behaviour consistent with matrix softening. As the matrix approaches the glass transition region, the load transfer efficiency decreases, promoting buckling/kinking type instability (with less pronounced delamination). This temperature sensitivity is particularly relevant given the application temperature of up to +150 °C and the comparatively low T_g measured for DC.

According to the minimum compression requirement reported in the material TPS (minimum compressive strength $\geq 290\,MPa$, and minimum compressive modulus $\geq 80\,GPa$),

both BC and DC satisfy the minimum compression criteria (see Table 2.2). This indicates that despite the undercured state of the DC batch, the measured compression properties remain above the TPS minima under the investigated test conditions, including at $T = 120$ °C.

Low-velocity impact and CAI tests confirmed the expected progressive reduction in residual compressive strength with increasing severity of the impact, and provided a broad mapping of impact response for DC through the 13 energy level campaign. At room temperature, the greater decrease in F_{CAI} occurs at low to moderate impact energies, where the impactor creates critical damage that strongly compromises residual stability; in this regime, the critical force for the onset of damage is independent of the impact energy. At higher energies ($E_i > 14$ J), the residual strength tends to level off around 111–120 MPa, consistent with damage saturation. Once delamination has effectively "saturated" the specimen, additional energy is increasingly expended in friction and penetration processes rather than further reducing residual compressive stability.

A direct batch comparison at matched energies shows two regimes at room temperature: at moderate impact energy ($E_i = 9.5$ J), BC and DC exhibit essentially identical residual strengths (141.9 MPa vs 142.8 MPa). This is consistent with both laminates operating well below their respective T_g and maintaining sufficient matrix stiffness to sustain load transfer and constrain instability. At higher severity impacts ($E_i = 18$ J), BC retains a higher residual strength (137.5 MPa) than DC (119.8 MPa), corresponding to a 13% reduction for the undercured batch. This separation highlights a greater susceptibility of DC to matrix/interface-controlled damage under severe impacts. This comparison must acknowledge that the 18 J conditions were not strictly matched in mass/velocity combination (higher velocity for BC, higher mass/lower velocity for DC), which can change contact duration, and thus damage footprint.

The high temperature CAI results for DC at 120 °C show a systematic reduction relative to room temperature ($\sim 10 - 20\%$ throughout all impact energies). This is consistent with matrix softening, which reduces interlaminar load transfer and the ability to restrain delamination-driven instability. The energy dependence remains similar: the largest decrease occurs between 0 and 9.5 J (from 193.5 MPa to ∼118 MPa), while at higher energies ($E_i > 14$ J) the residual strength tends to level off around 97–108 MPa.

The combined evidence demonstrates that the interruption of cure produced a measurable and structurally relevant undercure in DC. This is captured most clearly by (i) a higher residual cure enthalpy and a lower degree of cure; (ii) a strongly depressed and more variable T_g (DC ≈140 °C vs BC ≈180 °C); and (iii) a large through-thickness α_r with

high scatter. Although the room temperature mechanical properties analysed remain acceptable, the reduced thermal margin for DC is critical for aerospace operation at elevated temperature, and the undercure becomes more evident as the matrix approaches its transition region (compression and CAI at 120 °C).

To further consolidate and extend the present discoveries and to support full material qualification, the following research directions are proposed.

Matched testing is recommended to improve comparability and quantify the influence of the test methodology. This includes adopting a consistent technique for the determination of T_g, performing compression tests using the same standard and fixture for both BC and DC, and conducting impact tests with matched mass/velocity combinations. These steps would clarify how much of the observed differences can be attributed to the material state vs. the test configuration.

Considering that penetration and perforation thresholds depend on the size and geometry of the impactor (with P_n and P_r reported to increase linearly with impactor size [48]), a dedicated study is also suggested on the effect of different impactor geometries. This would help generalize the energy profile results and threshold values beyond the single striker configuration used in this work.

Future tests should also include high-temperature mechanical characterization of the BC batch, specifically compression and CAI at 120 °C, to enable a direct batch-to-batch comparison under elevated temperature conditions.

Regarding compression fracture analysis, one possible advance could be the microscopic study of fracture surfaces at both room and high temperatures. This would more clearly highlight the differences explained in Section 3.5.

In addition, the relationship between the degree of cure and long-term environmental resistance remains to be explored. Further studies should evaluate how cure variations affect ageing behaviour and moisture absorption.

The present work focused on strength and stiffness; however, structural reliability also depends strongly on fracture resistance. For this reason, the influence of the cure cycle on interlaminar fracture toughness (Mode I and Mode II) should be investigated.

Finally, future work could integrate Non Destructive Evaluation (NDE) with the thermochemical and mechanical results, to correlate the cure state with the internal defect morphology and the impact damage extent.

Bibliography

[1] Sharun Hegde, B. Satish Shenoy, and K. N. Chethan. Review on carbon fiber reinforced polymer (cfrp) and their mechanical performance. *Materials Today: Proceedings*, 19:658–662, 2019.

[2] Sanjay Mazumdar. *Composites Manufacturing*. CRC Press, 2001. ISBN 9781420041989, 1420041983.

[3] C. Soutis. Fibre reinforced composites in aircraft construction. *Progress in Aerospace Sciences*, 41(2):143–151, February 2005.

[4] T. D. Burchell. *Carbon Materials for Advanced Technologies*. Elsevier, 1999. ISBN 9780080528540, 0080528546.

[5] Ever J. Barbero. *Introduction to Composite Materials Design*. CRC Press, 2017. ISBN 9781315296487, 1315296489.

[6] Jean-Pierre Pascault and Roberto J. J. Williams. *Epoxy Polymers*. John Wiley & Sons, 2009. ISBN 3527628711, 9783527628711.

[7] Anqi Dong, Yan Zhao, Xinqing Zhao, and Qiyong Yu. Cure cycle optimization of rapidly cured out-of-autoclave composites. *Materials*, 11(3):421, March 2018.

[8] S. Alavi-Soltani, S. Sabzevari, H. Koushyar, and B. Minaie. Thermal, rheological, and mechanical properties of a polymer composite cured at different isothermal cure temperatures. *Journal of Composite Materials*, 46(5):575–587, August 2011.

[9] C. Gernaat, S. Alavi-Soltani, M. Guzman, A. Rodriguez, and B. Minaie. Correlation between viscoelastic and mechanical properties for an out-of-autoclave polymer composite. In *International SAMPE Technical Conference*, 2009.

[10] S. L. Agius, K. J. C. Magniez, and B. L. Fox. Cure behaviour and void development within rapidly cured out-of-autoclave composites. *Composites Part B: Engineering*, 47:230–237, April 2013.

[11] Nourredine Amdouni, Henry Sautereau, Jean-François Gérard, and Jean-Pierre Pas-

cault. Epoxy networks based on dicyandiamide: effect of the cure cycle on viscoelastic and mechanical properties. *Polymer*, 31(7):1245–1253, July 1990.

[12] S. R. White and H. T. Hahn. Process modeling of composite materials: Residual stress development during cure. part ii. experimental validation. *Journal of Composite Materials*, 26(16):2423–2453, January 1992.

[13] Peng Li, Xiaoping Yang, Yunhua Yu, and Dingsheng Yu. Cure kinetics, microheterogeneity, and mechanical properties of the high-temperature cure of vinyl ester resins. *Journal of Applied Polymer Science*, 92(2):1124–1133, February 2004.

[14] Nassim Rahmani, Bethany Willard, Kevin Lease, Ephriem T. Legesse, Seyed A. Soltani, and Suresh Keshavanarayana. The effect of post cure temperature on fiber/matrix adhesion of t650/cycom5320-1 using the micro-droplet technique. *Polymer Testing*, 46:14–20, September 2015.

[15] M. O. W. Richardson and M. J. Wisheart. Review of low-velocity impact properties of composite materials. *Composites Part A: Applied Science and Manufacturing*, 27 (12):1123–1131, 1996.

[16] S. Abrate. Impact on laminated composite materials. *Applied Mechanics Reviews*, 44(4):155–190, 1991.

[17] W. J. Cantwell and J. Morton. The impact resistance of composite materials—a review. *Composites*, 22(5):347–362, 1991.

[18] Jang-Kyo Kim and Man-Lung Sham. Impact and delamination failure of woven-fabric composites. *Composites Science and Technology*, 60(5):745–761, April 2000.

[19] D. Liu. Impact-induced delamination—a view of bending stiffness mismatching. *Journal of Composite Materials*, 22:674–692, 1988.

[20] *M46J High Modulus Carbon Fiber: Technical Data Sheet*. Toray Composite Materials America Inc., April 2025. URL `https://www.toraycma.com/wp-content/uploads/M46J-Data-Sheet.pdf`.

[21] *Toray TC250: Product Data Sheet*. Toray Advanced Composites, 18255 Sutter Blvd. Morgan Hill, CA 95037, USA, August 2020. URL `https://www.toraytac.com/media/486fa8ce-84e3-456e-a128-47208cab070d/eC139Q/TAC/Documents/Data_sheets/Thermoset/UD%20tapes%20and%20prepregs/TC250_Epoxy_PDS.pdf`.

[22] ASTM International. *ASTM D5687-02: Standard Guide for Preparation of Flat Composite Panels with Processing Guidelines for Specimen Preparation*, 2002.

[23] ASTM International. *ASTM D3418-15: Standard Test Method for Transition Temperatures and Enthalpies of Fusion and Crystallization of Polymers by Differential Scanning Calorimetry*, 2015.

[24] ASTM International. *ASTM E831-06: Standard Test Method for Linear Thermal Expansion of Solid Materials by Thermomechanical Analysis*, 2006.

[25] ASTM International. *ASTM E1545-16: Standard Test Method for Assignment of the Glass Transition Temperature by Thermomechanical Analysis*. West Conshohocken, PA, 2016.

[26] IPC. *Glass Transition Temperature and Thermal Expansion of Materials Used in High Density Interconnection (HDI) and Microvias – TMA Method*. IPC (Association Connecting Electronics Industries), Northbrook, IL, USA, November 1998. Test Methods Manual.

[27] Ashraf Ahmed, Behrouz Tavakol, Rony Das, Ronald Joven, Pooneh Roozbehjavan, and Bob Minaie. Study of thermal expansion in carbon fiber-reinforced polymer composites. In *SAMPE International Symposium Proceedings*, 2012.

[28] J. Foreman, S. R. Sauerbrunn, and C. L. Marcozzi. Exploring the sensitivity of thermal analysis techniques to the glass transition. *International Polymer Science and Technology*, 38(6):29–36, 2018.

[29] TA Instruments. *Determining the Glass Transition Temperature of an Epoxy Molding Compound by Thermomechanical Analysis (TMA)*. TA Instruments, 2015. URL `https://www.tainstruments.com.cn/wp-content/uploads/TA387.pdf`.

[30] Cirlene Fourquet Bandeira, Sérgio Roberto Montoro, Elton Luiz Espindola, Edson Cocchieri Botelho, Michelle Leali Costa, and Maria Odila Hilário Cioffi. Comparison of glass transition temperature values of composite polymer obtained by tma and dsc. *Applied Mechanics and Materials*, 719–720:91–95, 2015.

[31] ASTM International. *ASTM D7028-15: Standard Test Method for Glass Transition Temperature (DMA T_g) of Polymer Matrix Composites by Dynamic Mechanical Analysis (DMA)*, 2015.

[32] ASTM International. *ASTM D3171-11: Standard Test Methods for Constituent Content of Composite Materials*. West Conshohocken, PA, 2011.

[33] ASTM International. *ASTM D695-15: Standard Test Method for Compressive Properties of Rigid Plastics*, 2015.

[34] Peter M. Wegner and Donald F. Adams. Verification of the combined load compression (clc) test method. Final Report DOT/FAA/AR-00/26, U.S. Department of Transportation, Federal Aviation Administration, Office of Aviation Research, Washington, DC, August 2000.

[35] Qasim S. Khan, M. Neaz Sheikh, and Muhammad N. S. Hadi. Tension and compression testing of fibre reinforced polymer (frp) bars. In *Proceedings of the Joint Conference of the 12th International Symposium on Fiber Reinforced Polymers for Reinforced Concrete Structures (FRPRCS-12) & the 5th Asia-Pacific Conference on Fiber Reinforced Polymers in Structures (APFIS-2015)*, pages 1–6, Nanjing, China, December 2015.

[36] *Universal Testing Machine Compliance*. Instron, 2020. URL `https://www.instron.com/wp-content/uploads/2024/07/compliance-correction.pdf`. Instron technical note / application guide.

[37] J. A. Gruber. Accurate data reduction for the uniaxial compression test. *Experimental Techniques*, 42(2):209–221, October 2017.

[38] S. R. Kalidindi, A. Abusaifeih, and E. El-Danaf. Accurate characterization of machine compliance for simple compression testing. *Experimental Mechanics*, 37(2):210–215, June 1997.

[39] ASTM International. *ASTM D7136/D7136M-20: Standard Test Method for Measuring the Damage Resistance of a Fiber-Reinforced Polymer Matrix Composite to a Drop-Weight Impact Event*. ASTM International, 2020.

[40] ASTM International. *ASTM D7137/D7137M-23: Standard Test Method for Compressive Residual Strength Properties of Damaged Polymer Matrix Composite Plates*. ASTM International, 2023.

[41] Cesim Atas and Onur Sayman. An overall view on impact response of woven fabric composite plates. *Composite Structures*, 82(3):336–345, February 2008.

[42] D. D. R. Cartié and P. E. Irving. Effect of resin and fibre properties on impact and compression after impact performance of cfrp. *Composites Part A: Applied Science and Manufacturing*, 33(4):483–493, April 2002.

[43] Dhaval B. Shah, Kaushik M. Patel, Shashikant J. Joshi, Bharat A. Modi, Arvind I. Patel, and Vishwajit Pariyal. Thermo-mechanical characterization of carbon fiber composites with different epoxy resin systems. *Thermochimica Acta*, 676:39–46, June 2019.

[44] Wang Shaoquan, Dong Shangli, Gao Yu, and Sun Yungang. Thermal ageing effects on mechanical properties and barely visible impact damage behavior of a carbon fiber reinforced bismaleimide composite. *Materials & Design*, 115:213–223, February 2017.

[45] Guangyong Sun, Wen Zuo, Dongdong Chen, Quantian Luo, Tong Pang, and Qing Li. On the effects of temperature on tensile behavior of carbon fiber reinforced epoxy laminates. *Thin-Walled Structures*, 164:107769, July 2021.

[46] Jingsong Chen, Guangwu Yang, Shoune Xiao, Dongdong Chen, Mingmeng Wang, and Lanxin Jiang. Effect of temperature and moisture composite environments on the mechanical properties and mechanisms of woven carbon fiber composites. *Polymer Composites*, 45(5):4618–4635, January 2024.

[47] João R. Correia, Marco M. Gomes, José M. Pires, and Fernando A. Branco. Mechanical behaviour of pultruded glass fibre reinforced polymer composites at elevated temperature: Experiments and model assessment. *Composite Structures*, 98:303–313, April 2013.

[48] Dahsin Liu. Characterization of impact properties and damage process of glass/epoxy composite laminates. *Journal of Composite Materials*, 38(16):1425–1442, August 2004.

[49] Metin Sayer, Numan B. Bektaş, Ersin Demir, and Hasan Çallioğlu. The effect of temperatures on hybrid composite laminates under impact loading. *Composites Part B: Engineering*, 43(5):2152–2160, July 2012.

[50] A. T. DiBenedetto. Prediction of the glass transition temperature of polymers: A model based on the principle of corresponding states. *Journal of Polymer Science Part B: Polymer Physics*, 25(9):1949–1969, September 1987.

[51] J. P. Pascault and R. J. J. Williams. Glass transition temperature versus conversion relationships for thermosetting polymers. *Journal of Polymer Science Part B: Polymer Physics*, 28(1):85–95, January 1990.

[52] Arturo Hale, Christopher W. Macosko, and Harvey E. Bair. Glass transition temperature as a function of conversion in thermosetting polymers. *Macromolecules*, 24 (9):2610–2621, April 1991.

[53] Ricky Hardis, Julie L. P. Jessop, Frank E. Peters, and Michael R. Kessler. Cure kinetics characterization and monitoring of an epoxy resin using dsc, raman spectroscopy,

and dea. *Composites Part A: Applied Science and Manufacturing*, 49:100–108, June 2013.

[54] Xun Wu and Michael R. Wisnom. Compressive failure strain of unidirectional carbon fibre composites from bending tests. *Composite Structures*, 304:116467, January 2023.

[55] Instron. A review of current in-plane composites compression testing methods & standards. Technical report, Instron Corporation, 2015.

[56] Jeffry S. Welsh and Donald F. Adams. Testing of angle-ply laminates to obtain unidirectional composite compression strengths. *Composites Part A: Applied Science and Manufacturing*, 28(4):387–396, 1997.

[57] E. Lackey, K. Spoo, C. Gill, and J. Vaughan. Comparison of properties from compression and tensile test standards – a case study from the development of a load and resistance factor design (lrfd) standard for pultruded composites. *Mechanics of Composite Materials*, page 115, 2010. University of Mississippi, USA; Owens Corning, USA.

[58] Christina C. Gedney et al. Comparison of ASTM standard compression test methods of graphite/epoxy composite specimens. In *Proceedings of the 32nd International SAMPE Symposium*, pages 1015–1024, April 1987.

[59] Arthur Wolfe and Michael Weiner. Compression testing – comparison of various test methods. In *Composites 2004*, pages 1–4. American Composites Manufacturers Association, 2004.

[60] Donald Adams and Jeffry S. Welsh. The wyoming combined loading compression (clc) test method. *Journal of Composites Technology and Research*, 19(3):123–133, 1997.

[61] G. Caprino. Residual strength prediction of impacted cfrp laminates. *Journal of Composite Materials*, 18(6):508–518, November 1984.